Elsevier Editorial System(tm) for Earth and Planetary Science Letters

Manuscript Draft

Manuscript Number: EPSL-D-18-00510R2

Title: Crustal rheology of southern Tibet constrained from lake-induced viscoelastic deformation

Article Type: Letters

Keywords: Viscosity, Elastic thickness, Paleoshorelines, Tibet

Corresponding Author: Mr. Maxime Simon Henriquet, M.D.

Corresponding Author's Institution: Université de Montpellier

First Author: Maxime Simon Henriquet, M.D.

Order of Authors: Maxime Simon Henriquet, M.D.

Abstract: We probe the rheology of the Tibetan lithosphere using the rebound that accompanied climate-driven lake level variations. At the modern decadal time scale, we used deformation around Siling Tso measured from InSAR. At the millennial time scale, we use Holocene paleoshorelines around Siling Tso and Zhari Nam Tso. We use chronological constraints from the literature and Digital Elevation Models to constrain their ages and geometry. We observe a small post-highstand subsidence of the area near the center of mass of the paleolake-load and a low-amplitude short-wavelength outer bulge. In the context of a model consisting of an elastic lid over a viscous channel with a rigid base, these observations preclude the existence of a thick low viscosity channel and require a thin elastic lid. Based on Monte Carlo inversion, we constrain the range of possible equivalent elastic thickness of the lid (<5 km), the viscosity (2x10^18 - 10^20 Pa.s) and thickness of the crustal channel (<10-20 km). By contrast, the modern data requires a stiffer lid with equivalent elastic thickness >20 km and a >20 km thick channel with lower crustal viscosity (<5x10^18 Pa.s). The different rheologies inferred at these different time-scales could be explained by a Burgers body rheology of the middle and lower crust, with a short-term viscosity of 1018 Pa.s and long-term viscosity of 10^20 Pa.s, or even better by vertical variations of viscosity. To illustrate the latter claim, we show that the observations at the decadal and Holocene time scales can be reconciled by assuming a low viscosity zone (10^18 Pa.s) at mid-crustal depth (between ~10 and 30 km depth) embedded in a higher viscosity crust (>10^20 Pa.s). In both cases, the interferences in space of the deformation signals induced by the lakes geometry, and in time through the viscoelastic response to the lake level variations results in limited distortion of the paleo-shorelines. While the elastic lid in the upper crust needs in any case to be thin (<10 km), the low amplitude distortion requires significant viscoelastic support from the lower crust and upper mantle; this explains the relatively high effective elastic thickness (>20 km) inferred in some previous studies of Holocene paleoshorelines. In the longer term, the effective elastic thickness of the lithosphere must drop asymptotically to the value of the elastic lid in the upper crust (<10 km); this explains the low effective elastic thickness derived from gravity studies.

Crustal rheology of southern Tibet constrained from lake-induced viscoelastic deformation

Maxime Henriquet [1,2], Jean-Philippe Avouac[1], Bruce G. Bills[3]

1 Geology and Planetary Science Division, California Insitute of Technology

2 Géosciences Montpellier, Université de Montpellier

3 Jet Propulsion Laboratory, California Institute of Technology

Corresponding author: Maxime Henriquet (maxime.henriquet@gm.univ-montp2.fr), Géosciences Montpellier, Place Eugène Bataillon, 34090 Montpellier, France

Abstract

We probe the rheology of the Tibetan lithosphere using the rebound that accompanied climate-driven lake level variations. At the modern decadal time scale, we used deformation around Siling Tso measured from InSAR. At the millennial time scale, we use Holocene paleoshorelines around Siling Tso and Zhari Nam Tso. We use chronological constraints from the literature and Digital Elevation Models to constrain their ages and geometry. We observe a small post-highstand subsidence of the area near the center of mass of the paleolake-load and a low-amplitude short-wavelength outer bulge. In the context of a model consisting of an elastic lid over a viscous channel with a rigid base, these observations preclude the existence of a thick low viscosity channel and require a thin elastic lid. Based on Monte Carlo inversion, we constrain the range of possible equivalent elastic thickness of the lid (<5 km), the viscosity ($2x10^{18}$ - 10^{20} Pa.s) and thickness of the crustal channel (<10-20 km). By contrast, the modern data requires a stiffer lid with equivalent elastic thickness >20 km and a >20 km thick channel with lower crustal viscosity (<$5x10^{18}$ Pa.s). The different rheologies inferred at these different time-scales could be explained by a Burgers body rheology of the middle and lower crust, with a short-term viscosity of 10^{18} Pa.s and long-term viscosity of 10^{20} Pa.s, or even better by vertical variations of viscosity. To illustrate the latter claim, we show that the observations at the decadal and Holocene time scales can be reconciled by assuming a low viscosity zone (10^{18} Pa.s) at mid-crustal depth (between ~10 and 30 km depth) embedded in a higher viscosity crust (>10^{20} Pa.s). In both cases, the interferences in space of the deformation signals induced by the lakes geometry, and in time through the viscoelastic response to the lake level variations results in limited distortion of the paleo-

shorelines. While the elastic lid in the upper crust needs in any case to be thin (<10 km), the low amplitude distortion requires significant viscoelastic support from the lower crust and upper mantle; this explains the relatively high effective elastic thickness (>20 km) inferred in some previous studies of Holocene paleoshorelines. In the longer term, the effective elastic thickness of the lithosphere must drop asymptotically to the value of the elastic lid in the upper crust (<10 km); this explains the low effective elastic thickness derived from gravity studies.

Keywords: Viscosity, Elastic thickness, Time-dependent, Paleoshorelines, Tibet

1 Introduction

The rheological stratification of the continental crust remains a subject of debate (e.g., Bürgmann & Dresen, 2008; Burov & Watts, 2014; Jackson, 2002). This debate is central to our understanding of continental tectonics, the formation and evolution of mountain ranges and orogenic plateaus in particular (e.g., Beaumont *et al*., 2001; Copley *et al*., 2011) and of the seismic cycle (e.g., Hilley *et al*., 2009; Huc *et al*., 1998; Johnson & Segall, 2004).

It has long been suspected that the thick Tibetan crust is particularly weak. A low viscosity crust (<10^{19} Pa.s) and small elastic thickness (<10 km) would indeed explain the relatively flat topography of Tibet (Zhao & Morgan, 1987; Masek *et al*, 1994). Relatively

46 low viscosities are expected given the high crustal temperatures that must have resulted
47 from the ~70 km thick radiogenic continental crust (*e.g.*, Wang *et al.*, 2013). Partial
48 melting and a low velocity zone suggesting a weak lower crust have also been inferred
49 from geophysical studies (Klemperer, 2006; Nelson *et al.*, 1996; Unsworth *et al.*, 2005).
50 Some authors have argued for "channel flow" invoking a very weak and laterally mobile
51 lower crust. For instance, a large horizontal flux of middle and lower crust squeezed out
52 from beneath the plateau could explain some aspect of the morphology and tectonics of
53 eastern Tibet and the Himalaya (Beaumont *et al.*, 2001; Clark & Royden, 2000). Such
54 channel flow tectonics would imply a viscosity possibly as low as 10^{17} Pa.s (e.g., Clark *et*
55 *al.*, 2005; Royden *et al.*, 1997). However, several geological and geophysical data seem
56 inconsistent with such a weak lower crust. Seismic anisotropy observations suggest
57 coherent deformation throughout the eastern Tibetan lithosphere and hence little
58 decoupling at mid-crustal depth (León Soto *et al.*, 2012). The contrast between the
59 northern part of the plateau, which is dominated by strike-slip faulting, and the southern
60 part, dominated by normal faulting is also an evidence for a strong coupling between the
61 lower crust and upper mantle in southern Tibet (Copley *et al.*, 2011).

62 Direct constraints on the rheology of the lithosphere may be derived from observing a
63 time-dependent deformation response to a known stress perturbation. At the decadal
64 timescale the viscosity can be estimated from postseismic observations following large
65 earthquakes. Such studies have yielded values between 10^{17} Pa.s to more than 10^{21} Pa.s
66 (Hilley *et al.*, 2005; Huang *et al.*, 2014; Ryder *et al.*, 2011; Ryder *et al.*, 2014; Yamasaki
67 & Houseman, 2012; Zhang *et al.*, 2009). A significant source of uncertainties in such
68 studies is due to the fact that it is difficult to separate the contributions of afterslip and

69 viscous relaxation to postseismic deformation. In addition, we do not know whether
70 viscous relaxation beneath the seismogenic zone is broadly distributed or localized. The
71 rheology inferred from postseismic studies might therefore not be representative of the
72 bulk rheology of the crust.

73 Crustal rheology may alternatively be probed from the surface deformation induced by
74 lake level variations (Bills *et al*, 1994; Kaufman & Amelung, 2000). For instance Doin *et*
75 *al*., 2015 studied the Siling Tso example (Figure 1a). The water level has been rising up
76 recently by about 1 meter per year, flexing down the topography around it. According to
77 Doin *et al*. (2015), the model that best fits the deformation signal measured from InSAR
78 has an elastic upper crust with an equivalent elastic thickness (*Te*) of ~30 km and a lower
79 crust with a viscosity of 1-3x10^{18} Pa.s. It is also possible to estimate the rheology of the
80 crust at the millennial time scale based on surface deformation resulting from lake level
81 fluctuations induced by late Quaternary climate change (e.g., Bills *et al*., 1994; 2007).
82 This method has also recently been used in Tibet where numerous closed basins bear
83 well-preserved paleoshorelines (England *et al*., 2013; England & Walker, 2016; Shi *et al*.,
84 2015). Surprisingly, the paleoshorelines are hardly distorted implying either a large
85 equivalent elastic thickness ($\geq$ 25 km) or a high viscosity crust ($\geq 10^{19}$ Pa.s).

86 In this study, we re-analyse and seek to reconcile the rheology inferred from the lake-
87 induced deformation signal at the decadal and millennial time scales. The motivations for
88 the re-analysis are multiple. Firstly, the trade-off between the equivalent elastic thickness
89 of the crust and the thickness and viscosity of the viscous channel was not fully explored
90 in previous studies. Secondly, previous studies have assumed very simple paleo-lake
91 level variations which can now be refined based on recent studies of Tibet paleolakes

92 (Ahlborn *et al*., 2016; Chen *et al*., 2013; Hudson *et al*., 2015; Lee *et al*., 2009; Rades *et*
93 *al*., 2015; Shi *et al*., 2017). Thirdly, the possible effect of loading and unloading by
94 mountain glaciers was ignored in previous studies; there is however clear geomorphic
95 evidence that the mountain ranges around these lakes underwent glacial advances.
96 Finally, there are now good quality images and better DEMs which can be used to
97 measure the distortion of the paleoshorelines more extensively.

98

99 ## 2 Deformed paleoshorelines and Holocene loads

100 ### 2.1 Previous results inferred from lake-induced deformation in Tibet

101 At the modern decadal time scale Doin *et al*., 2015 studied the ground deformation due to
102 Siling Tso level rise of 1.0 m/yr from 2000 to 2006. They measured the ground
103 deformation using interferometric synthetic aperture radar (InSAR) for the 1992-2011
104 period. Their models considered a crust consisting of an upper elastic lid over a
105 viscoelastic channel adding to an imposed thickness of 65 km. Here, we revisit their
106 analysis by allowing the thickness of the viscoelastic channel to be independent of the
107 elastic lid thickness. The rationale is that the lower crust could be granulitic and rather
108 cold due to the effect of underthrusting of India on the thermal structure and might
109 therefore not be part of the low viscosity channel.

110

111 Late Pleistocene to Holocene paleoshorelines are widespread all over Tibet (*e.g*., Gasse *et*
112 *al*., 1991, Ahlborn *et al*., 2016; Avouac *et al*., 1996; Chen *et al*., 2013; England *et al*.,
113 2013; Hudson *et al*., 2015; Lee *et al*., 2009; Rades *et al*., 2015; Shi *et al*., 2015). Five
114 major closed-basin lake systems in the central part of the plateau have already been

115 studied to constrain rheological properties of the Tibetan crust (England *et al*., 2013;
116 England & Walker, 2016; Shi *et al*., 2015). The Ngangla Ring Tso, Taro Tso, Zhari Nam
117 Tso and Tangra Yum Tso were studied by England *et al*., 2013 whereas Shi *et al*., 2015
118 analysed the shorelines around Siling Tso (Figure 1a). The paleoshorelines were
119 measured using Shuttle Radar Topographic Mission elevations combined with Google
120 Earth imagery of shorelines and some kinematic GPS measurements around the Zhari
121 Nam Tso (England *et al*., 2013). These lakes are among the largest in Tibet and filled up
122 to 150-200 m above their present level in the Holocene. A large deformation response to
123 unloading might therefore have been expected, but no conspicuous deformation signal
124 was found at any of them. The shorelines are distorted from horizontality by no more
125 than ~10 m. These observations place important constraints on the rheology of the Tibet
126 crust, but the previous studies leave room for some reanalysis. These studies neglected
127 the potential effects of surrounding glacial unloading, the simulated lakes level histories
128 were very simplified and the small datasets were too sparse to detect short-wavelength
129 distortion. We therefore revisit this problem with more complete load scenarios and an
130 augmented dataset of shoreline elevations that we produced using satellite images.
131

132 ## 2.2 Geomorphology of Holocene paleoshorelines

133 We focused on the best-preserved, presumably most recent shorelines, which also have
134 the best-constrained loading history. Those formed on gentle alluvial slope, such as the
135 ridges seen in Figure 1b, are not very durable and probably of Holocene age in the
136 context of Tibet. The highest stand of the Zhari Nam Tso preserved in the morphology
137 has been found to postdate the Last Glacial Maximum (e.g., Kong *et al*., 2011). Field

138 observations show that they commonly form couplets, separated in height by ~0.5-1 m,
139 which could reflect a seasonal effect (England *et al*., 2013). The elevation of a particular
140 shoreline can vary laterally but generally within less than 0.5 m (Shi *et al*., 2015).
141 Therefore, the intrinsic variability of shoreline elevation is estimated to be of the order of
142 ~1 m.
143
144 We used ~2.5 m ground resolution satellite images to pick the highest well-preserved
145 shorelines visible on alluvial surfaces around Zhari Nam Tso and Siling Tso (Figure 1b
146 and Figure 2). Their elevations is estimated by sampling the global DEM ALOSWorld
147 3D - 30m (AW3D30) released in 2015 by the Japan Aerospace Exploration Agency
148 (JAXA) using a bicubic interpolation. We selected only paleoshorelines located on gentle
149 slopes, based on our visual assessment, to minimize elevation errors due to the possible
150 misregistration of the images to the DEM (Figure 1b). A posteriori quantitative slope
151 analysis at the location of these measurements shows that for the 1914 samples around
152 Zhari Nam Tso, 66% are located on slopes < 5° and 94% on slopes < 10°. Similarly on
153 the 474 samples on Siling Tso paleoshorelines, 89% are on slopes < 5° and 100% are <
154 10° (see Appendix A of supplements for details).
155
156 The mean elevation of the highest shoreline around Siling Tso is ~4597 m and ~4751 m
157 for Zhari Nam Tso (histograms of Figures 3a and 3b). The red histograms Figure 3 a and
158 b show the distribution of the difference between the raw and the filtered elevations data
159 which were smoothed using a 10 km square sliding window. These approximately normal
160 distributions are used to characterize the noise on shoreline elevations. We estimate the

67% uncertainties on shoreline elevation to ~1.5 m at both Siling Tso and Zhari Nam Tso. The distribution of elevations smoothed at the 10 km scale reveal a variability (~6 m for each datasets) that exceeds this uncertainty. Given that we do not expect the noise on shorelines elevation to correlate at length scales larger than 10km, we interpret this pattern as a real deformation signal. The significance of this signal is not immediately intuitive however. It does not show the typical "bowl shape" uplift pattern centered on the centroid of the water load which would be expected from a simple elastic rebound. The central part of the Siling Tso basin was apparently deflected downward, whereas uplift would have been expected in that area of maximum unloading. This central zone of subsidence is fringed by an outer bulge of uplift which is a few tens of kilometers wide. The Zhari Nam Tso shorelines show a similar pattern, though more complicated probably due the more contorted geometry of the paleolake and the interference with the nearby lakes.

We characterize the wavelength of the deformation signal using the standard deviation of the paleoshoreline elevations within a sliding square window of varying size between 0 to 100 km (Figure 3 c and d). We use the filtered data (obtained by averaging within a 10 km x 10 km wide sliding window) as this filtering helps comparison with the model predictions which have no noise. Windows with less than 20 data (chosen arbitrarily) were discarded to filter out poorly constrained values. The standard deviation of both datasets increases rapidly with the window size up to ~70-80 km for Siling Tso and Tso ~60 km for Zhari Nam Tso and levels off for larger windows. It suggests that the deformation signal has a wavelength of the order of ~60-80 km, smaller than the

184 wavelength expected from the rheological models derived from previous studies (Shi *et*
185 *al*., 2015; Doin et al, 2015) (Figure 3 c and d).
186
187 ## 2.3 Lakes level variation over the Holocene
188 A number of paleoclimatic studies have documented the timing of the highstand and of
189 the regression of the lakes analyzed in this study (Ahlborn *et al*., 2016; Chen *et al*., 2013;
190 Hudson *et al*., 2015; Lee *et al*., 2009; Rades *et al*., 2015; Shi *et al*., 2017). Siling Tso
191 (Figure 1d) reached its highstand probably at ~10 ka and started to regress progressively
192 to its present-day level at ~4 ka, possibly due to weakening of the monsoon (Shi *et al*.,
193 2017). The three lakes around Zhari Nam Tso (Ngangla Ring Tso, Taro Tso and Tangra
194 Yum Tso) followed a slightly different history (Figure 1c). They also reached their
195 highstand after the Last Glacial Maximum and maintained a highstand during the early
196 Holocene climatic optimum (Figure 1c) when rainfall was more abundant than at present
197 but started to regress earlier than Siling Tso at ~8.5 ka (Hudson *et al*., 2015). This time
198 evolution is somewhat different from the abrupt regression at ~5 ka assumed by England
199 *et al*., 2015. The lack of data for the early Holocene and Late Pleistocene makes it
200 difficult to estimate when the lakes reached their highstand. The available data show
201 disparities that might reflect a variable contribution from ice melting depending on the
202 particular setting of each basin. For simplicity, we assume that all four lakes around Zhari
203 Nam Tso followed the same time evolution represented by a post LGM highstand plateau
204 of variable duration, t_h, and a gradual regression starting at 8.5 ka (Figure 1c).
205

To estimate the load induced by the five paleolakes, we extracted the contour lines corresponding to their mean highstand elevation (Ngangla Ring Tso: 4864 m, Taro Tso: 4606 m, Zhari Nam Tso: 4751 m, Tangra Yum Tso: 4741 m and Siling Tso: 4597 m). The difference between the highstand and the local ground elevation within each basin provide an estimate of the spatial distribution of the drop of surface load that resulted from the lake regression. This estimate can be corrected from the post-regression rebound with a few model iterations.

2.4 Variation of glacial extent

Well-preserved moraines are observed at the outlet of most valleys carved into the ranges surrounding the lakes. The major glacial advance preserved in Central Tibet probably occurred in the early Holocene (Owen & Dortch, 2014). If so, these mountain glaciers might have contributed to the deformation of the Holocene paleoshorelines. We therefore estimated the surface load variations that would have resulted for the glacial retreat following the maximum extent preserved in the morphology. To do so, we used the Gc2d thin-sheet ice model of Kessler *et al*. (2006) (Appendix B). This 2-dimensional numerical model simulates the growth of glaciers for a given topography and meteorology. Using an explicit finite difference scheme by solving ice flux and mass conservation equations the model returns the ice elevation distribution through time. We estimated a lower and upper bound of glacial extent, and a medium case (Supplementary Figure B.1).

3 Modeling

3.1 Forward modeling

229 To model the distortion of the shorelines different simplified representations of the
230 rheology of the crust were considered. A number of analytical solutions allow calculating
231 the elastic or visco-elastic deformation of a layered planar earth model submitted to a
232 time-dependent vertical load at the surface. We first consider an elastic thin plate over an
233 inviscid fluid to estimate the asymptotic deformation response expected after complete
234 viscous relaxation. We use the analytical solution of Brotchie & Silvester, 1969
235 (Equation C.2, Appendix C). The viscoelastic response is calculated using the approach
236 of Nakiboglu & Lambeck, 1982 (Equation C.3 and C.4, Appendix C). It assumes an
237 elastic lid over a channel with a Maxwell rheology and a rigid base. The impact and
238 significance of rigid base assumption is discussed below. These analytical solutions can
239 be used to describe the response to any instantaneous variation of surface load. The load
240 history is simulated by discretizing the time variations of surface load as a series of step
241 functions.
242
243 We run the models forward based on the assumed lake level history and then compare the
244 observed and predicted distortions of the paleoshorelines elevation. Given a surface load
245 history, which is estimated based on the present topography and the assumed lake level
246 variations, the models allow predicting vertical displacements that would have affected
247 an initially undeformed horizontal shoreline at the onset of the lake regression.
248 As a first step, we adopt the same approach as England *et al*., 2013 for the purely elastic
249 case. We vary the elastic thickness *Te* from 1 to 40 km and compare the measured
250 difference of elevation between the maximum and the minimum elevation of the
251 paleoshorelines (~6 m) with the range of vertical displacements. This approach makes

252 sense if the spatial variations of paleoshorelines elevations reflect measurement errors
253 rather than a true pattern of vertical displacement. If the spatial pattern is a real
254 deformation signal, it is then more appropriate to compare the observed and the modeled
255 distortions at the location of the data. The models can be tested by retrodeforming the
256 paleoshorelines, *i.e.*, by subtracting the predicted uplift from the present elevation at each
257 data point. The best models are those which best restore the paleoshorelines to
258 horizontality. A natural goodness of fit criterion is therefore the standard deviation of the
259 retrodeformed elevations.
260
261 A model output is the estimated mean elevation of the paleoshoreline at the time of
262 deposition (Z_0). This information can then be used to correct the initial estimated load.
263 We initially started with estimating the load based on the elevation of the paleoshorelines
264 above the present lake level. This estimate ignores the distortion of the paleoshorelines.
265 The load can be re-estimated based on the mean elevation of the paleoshoreline above the
266 retrodeformed topography. The model can thus be adjusted iteratively until it is self-
267 consistent. Fewer than 5 iterations are sufficient to obtain a convergence within 0.1 %
268 with the purely elastic models. As a result of these iterations 10 to 20 % of additional
269 uplift is predicted. However these iterations are not used in the inversions procedure
270 described below due to their computational cost and their second order effect on the
271 surface response to load regression.
272

273 ## 3.2 Goodness of fit criterion

We define here the goodness of fit criterion used to quantify the discrepancy between the model predictions and the observations. The analytical calculation returns vertical displacement values M relative to the initial horizontal highstand at elevation Z_0 which is a priori unknown. The predicted distortion M(x,y) should equal $Z_{obs}(x,y) - Z_0$. It follows that, for each location $Z_{obs}(x,y) - M(x,y)$ is the estimated initial highstand elevation Z_0. The best model is the one that restores best the paleoshoreline to horizontality, so the one which minimizes $Z_{obs}(x,y) - M(x,y) - < Z_{obs} - M >$, where < > is the arithmetic average. Thus the best fitting model corresponds to the one that minimizes the dimensionless reduced Chi-square

$$\chi_r^2 = \frac{1}{(n-p)\sigma^2} \sum^{n} [Z_{obs}(x,y) - M(x,y) - < Z_{obs} - M >]^2 \quad (1)$$

where n is the number of observations, p the number of varying parameters and σ the standard deviation.

The best estimate of the highstand mean elevation Z_0 is $< Z_{obs} - M >$ that is thus a model output. A model that fits the data within uncertainties yields a χ_r^2 value of the order of unity. Chi-squared statistics can then be used to estimate the uncertainties on the model parameters.

3.3 Inversion

The adjustable parameters in our inversions are, the thickness Te of the elastic lid, the thickness L and viscosity η of the underlying viscous channel and the highstand duration t_h (for Zhari Nam Tso only). We explore the space of model parameters using a Monte

295 Carlo method with the built-in matlab *slicesample* function (Neal, 2003). This procedure
296 results in a higher density of samples in regions of lower misfit.
297
298 # 4 Results
299 ## 4.1 Elastic flexure
300 We first consider the case of an elastic layer of thickness *Te* over an inviscid fluid (Figure
301 4a). The surface load can be related to the lakes alone or the lakes and the surrounding
302 glaciers. This model gives an estimate of the elastic thickness *Te* which is necessary to
303 support the load with elastic stresses only. As viscous support is ignored, *Te* estimated in
304 this way should be considered as an upper bound. For simplicity we assume that loading
305 by glaciers and lakes is synchronous. This is not realistic as these two types of loads must
306 have had a different time history. The calculation does, however, quantify the possible
307 effect of the glaciers on the shoreline distortion. Figure 4a compares the maximum
308 distortion derived from the mapped paleoshorelines around Zhari Nam Tso, with the
309 distortion predicted in response to the lakes regression with, or without the effect of the
310 glaciers retreat. Figure 4b shows the spatial distribution of vertical rebound for Te = 10
311 km, at the lower end of the values proposed by England *et al*., 2013. As expected, we see
312 local maxima of the rebound near the centers of the paleolakes. Neighboring lakes do not
313 interfere much in that case. They start to influence each other for larger values of *Te*. The
314 flexural parameter is about 23 km in that case and it increases as $Te^{0.75}$ (see relationships
315 between *Te* and β in Table C.1). The observation of no more than ~6 m of distortion
316 requires $Te \geq 35$ km, a lower bound consistent with the results of England *et al*., 2013 and
317 Shi *et al*., 2015. The lower bound is even larger value if the effect of glaciers retreat is

318 included (Figure 4a). Glacial unloading has little effect for *Te* <10 km because most of
319 the surrounding glaciers are >185 km away from the paleoshorelines. By contrast, if *Te*
320 >10 km, the glaciers could potentially have an effect on the shoreline distortion. We
321 conclude that the influence of the glaciers is probably very small and does not help
322 explain the short wavelength and low amplitude distortion of the paleoshorelines.
323

324 ## 4.2 Viscoelastic flexure

325 A load history is required in viscoelastic models. For Zhari Nam Tso and the 3 lakes
326 around we assume a linear regression from 8.5 ka to present (Figure 1c). We use the
327 Zhari Nam Tso example to assess the effect of the duration of the highstand, t_h, which
328 could be of the same order of magnitude as the relaxation time. The time when the lakes
329 reached their highstand is varied between 10 ka and 20 ka, which gives a highstand
330 duration t_h of 1.5 ky to 11.5 ky. In absence of reliable time constraints on the glacial
331 history, we assume that the glaciers grew from 26 ka to 24 ka and that they retreated as
332 the lakes were gaining volume, presumably suppllied by glaciers melting. Our results,
333 detailed below, show that the duration of the highstand does not trade off with any other
334 model parameters. So we did not include the duration of the highstand as a parameter in
335 the case of Siling Tso. For the Holocene history of Siling Tso (Figure 1d), we assume a
336 linear rise of the lake level from 10.5 ka to 9.5 ka and a regression from 4 ka to present.
337 The duration of the highstand is fixed to 5.5 ky. Finally, the Siling Tso is assumed to
338 have risen by 10 m approximately from 2000 to 2006 based on Doin *et al*., 2015.
339

We first compare the paleoshorelines observations with the predictions from the preferred model of Doin *et al*., 2015 derived from the deformation response to the modern rise of Siling Tso (Figure 4c). We did not use the original raw InSAR data as it would have entailed redoing the analysis in its entirety including the implementation of a non-standard procedure to separate the signal from the noise. So our analysis assumes that the best-fitting model of Doin *et al*., 2015 (Supplementary Figure F.1) is a valid model within the parameter space that was explored in this study. This model has an elastic lid of thickness Te = 30 km overlying a viscoelastic channel of thickness L = 35 km and of viscosity $\eta = 2.10^{18}$ Pa.s over a rigid base. At Zhari Nam Tso it predicts a distortion of less than 6 m, a value consistent with the paleoshorelines measurements. The reduced Chi-square corresponding to this model, without the glaciers, is ~2.3. Like the purely elastic model, this viscoelastic model fails to fit the observed short-wavelength distortion pattern. The wavelength associated with this model is much larger than ~60-80 km, as a result the standard deviation of the distortions increases nearly linearly with the window size over the range of tested values (0 to 100 km, Model 3 in Figure 3d) contrary to what the data show.

The Monte Carlo search for the best set of parameters starts from an initially random set of parameters within a defined range: $\eta = 10^{17}$ - 10^{21} Pa.s, L = 1 - 50 km, Te = 1 - 30 km and for Zhari Nam Tso t_h = 1.5 - 11.5 ky. Figure 5 displays the misfit (reduced Chi-square, χ_r^2, Equation 1) for all the realizations associated to the inversion of Zhari Nam Tso paleoshorelines as a function of η and L, with panels corresponding to binned values of Te or t_h. The better models, with reduced χ_r^2 close to 1.82 fall in a domain defined by

363 an elastic thickness *Te* <10 km, a viscosity η of 10^{18} Pa.s to 10^{20} Pa.s and a channel
364 thickness *L* <10-20 km. The plot shows a strong trade-off between the channel thickness
365 *L* and viscosity η: a thicker channel requires a higher viscosity to maintain a comparable
366 fit to the data. Such a trade-off is expected as the relaxation time for channel flow is
367 $\tau \sim \frac{2\,\eta R^2}{\rho g L^3}$ (with *R* being the radius of the load or the elastic flexural parameter whichever is
368 larger, *L* the channel thickness, η the viscosity of the viscous medium and ρ its density).
369 The highstand duration t_h does not trade-off with any other model parameters in the range
370 of tested values (1.5 ky to 11.5 ky).
371
372 Figure 6 shows the result of the inversion of the paleoshorelines around Siling Tso
373 (labeled "mid-term", Figure 6a) and of the modern ground deformation (labeled "short-
374 term", Figure 6b). In the later case we use as an input in the inversion the vertical
375 displacements predicted by the best model of Doin *et al*., 2015 which fits all the InSAR
376 data used in the analysis within their uncertainties (Supplementary Figure F.1, data
377 provided as electronic supplement). Thus we try to determine models parameterized with
378 3 variables (elastic thickness, channel thickness and channel viscosity) equivalent to the
379 preferred model of Doin *et al*., 2015 which has only two independent parameters has an
380 elastic lid of thickness *Te* = 30 km overlying a viscoelastic channel of viscosity η =
381 $2\text{x}10^{18}$ Pa.s and thickness *L* = 65 - 30 = 35 km over a rigid base. At the millennial time
382 scale, the results are similar to those from Zhari Nam Tso (Figure 5). The plots in Figure
383 6a show a strong trade-off between the channel thickness and viscosity: a thicker channel
384 (from 10 km to 20 km) requires a higher viscosity (from 10^{18} Pa.s to 10^{19} Pa.s) to
385 maintain a comparable fit to the data (χ_r^2 ~6). However a small trade-off between the

386 channel viscosity and the elastic thickness is found at the Holocene time scale. The
387 inversion results at the decadal time scale are similar to those of Doin *et al*., 2015,
388 showing that the better models (normalized χ_r^2 ~1) have a rather large elastic thickness,
389 *Te* ~30 km, a relatively low viscosity, η <10^{19} Pa.s, and a channel thicknesses *L* >20 km.
390 In this case, a clear trade-off between *Te* and η shows that a thin elastic lid (*Te* ~10 km)
391 requires a viscosity one order of magnitude lower than for equivalent elastic thicknesses
392 *Te* ~30 km (Figure 6b) to maintain a comparable fit to the data (normalized χ_r^2 ~1).
393
394 Figure 2 compares the paleoshorelines observations and predictions for models selected
395 among the best fitting ones. For Siling Tso the model has: η = 1.8x10^{18} Pa.s, *L* = 9 km
396 and *Te* = 2 km. For Zhari Nam Tso it has: η = 5x10^{19} Pa.s, *L* = 6.4 km, *Te* = 5.9 km and t_h
397 = 5.23 ky. Given the small elastic thicknesses of these models, the glaciers have
398 insignificant impact on the paleoshorelines distortion. The comparison between the
399 measured and predicted elevations of paleoshorelines shows in fact a rather poor fit with
400 misfits mostly larger than the estimated 1.5 m uncertainty on the shoreline elevations as
401 reflected the large reduced Chi-squares values (Supplementary Figure E1). These models
402 do however predict distortions of the paleoshorelines with a short wavelength consistent
403 with the observations, though of lower amplitude (for Zhari Nam Tso particularly). These
404 models also predict subsidence at the center of the paleolakes, where the surface
405 unloading is maximum. So these models are able to reproduce qualitatively some key
406 features of the data but they fall short of fitting them quantitatively. Possible causes for
407 the misfits include: DEMs error with a correlation scale larger than 10 km; incorrect
408 hypothesis that the highest preserved shorelines around each lake are synchronous and

409 were initially horizontal; incorrect model due to spatial variations of visco-elastic
410 properties; incorrect load estimate because of changes of the topography and
411 redistribution of mass by erosion or sedimentation during the regression of the lakes; sub-
412 crustal deformation. Whatever the cause, the constraints on the rheology of the crust
413 derived above probably hold anyway.
414

415 # 5 Discussion

416 ## 5.1 Significance of the rigid base boundary condition

417 The boundary condition in these calculations is a rigid base, implying support from the
418 medium below the viscoelastic channel as discussed in England *et al*., 2013. As a result,
419 the shoreline distortions become negligible when the channel thickness tends to 0 km.
420 The best fitting models include this end-member and all require some minimum coupling
421 between the upper elastic lid and the rigid base at the Holocene time scale. Assuming a
422 rigid base is not realistic and subcrustal deformation could in fact have affected distortion
423 of the paleoshorelines. We have therefore carried out forward tests to evaluate the
424 possible contribution of this effect, using the viscoelastic code from Bills et al., 1994
425 which allows modeling a response of any vertically stratified viscoelastic Earth.
426

427 Figure 7 compares the surface deformation in the case of a subcrustal viscoelastic support
428 to the rigid base approximation. The models both assume an elastic lid of thickness Te =
429 2 km overlying an L = 9 km thick viscoelastic channel of viscosity $\eta = 1.8 \times 10^{18}$ Pa.s. One
430 model has a quasi-rigid base (modeled here with a viscosity of 10^{25} Pa.s) (Figure 7a) and
431 the other a 35 km thick sub-crustal elastic lid over a viscoelastic half-space of viscosity

10^{18} Pa.s (Figure 7b). The difference between these two models (Figures 7c and 7d) is a low amplitude (<2 m) and long-wavelength (>100 km) signal. The observation of limited deformation at the scale of the paleoshorelines footprint thus requires coupling of the upper crust with a strong sub-crustal viscoelastic lid at the millennial time scale. We haven't explored further the constraints placed on subcrustal rheology as there is probably a large trade off between viscous and elastic support which cannot be easily resolved with the data considered in this study.

If criterions of fit were the distortion range as in England *et al*., 2013, there would be a strong trade-off between the channel properties and substrate viscosity. A low substrate viscosity of 10^{21} Pa.s or less would then imply a higher channel viscosity than the values inferred from our inversions. However such models would not be able to produce the short-wavelength deformation of the paleoshorelines. This trade-off is much reduced if, as done in this study, the difference between the observed and predicted elevations at the actual location of the paleoshorelines measurements is minimized.

5.2 Trade-off between viscous and elastic support of surface loads

The short-term deformation response to Siling Tso lake level variations can be fitted equally well with dominantly either elastic or viscous support. This is clearly seen in the trade-off between the viscosity η and the elastic thickness *Te* (Figure 6b). By contrast, no such trade-off is seen in the results from the inversion of the paleoshorelines (Figures 5 and 6). Some insight is gained by considering purely elastic models. A simple model consisting of an elastic lid over an inviscid fluid could explain the insignificant

455 deformation of the shorelines as England *et al*., 2013 have found. However, the small
456 distortion (<6 m) of the paleoshorelines requires *Te* ~35 km. Such a large elastic
457 thickness is considerably higher than the *Te* ~10 km estimate deduced from gravity in the
458 studied area (Braitenberg *et al*., 2003). It is therefore likely that, at the millennial time
459 scale of the paleoshorelines deformation, surface loads are at least partially supported by
460 viscous stresses.
461

462 ## 5.3 Origin of the central downward distortion and upward bulge.

463 We investigate here the mechanism responsible for the short wavelength deformation of
464 the paleoshorelines and the lower elevations of the paleoshorelines nearer to the center of
465 the lakes despite being closer to the maximum unloading. These two non-intuitive
466 features are actually seen in the deformation pattern predicted by the best fitting models
467 (Figures 2 and 3). To gain insight we analyze the viscoelastic response predicted by our
468 model in the simple case of a single cylindrical load with a load history similar to the one
469 assigned to the Zhari Nam Tso (see simulations in Appendix D.1). Figure 8 illustrates
470 how viscous effects influence the wavelength, sign and amplitude of the vertical
471 displacements in space and time. The lake transgression induces a central zone of
472 subsidence fringed by a zone of uplift that diffuses away as a result of channel flow. The
473 opposite happens during regression and the two patterns interfere. For large enough
474 channel viscosities and a progressive unloading, the subsidence induced by the lake
475 highstand goes on during the early stage of surface unloading and can dominate the uplift
476 induced by the unloading. The model predicts a transition from subsidence to uplift after
477 some time that scales with the viscoelastic relaxation time. It takes then time before uplift

compensates the cumulated initial subsidence. Note that this mechanism does not imply that, at present, the ground would be still subsiding near the center of the paleolakes. This effect doesn't happen in the case of an abrupt lake regression as assumed in the study of England *et al*., 2013. Uplift then starts directly after unloading. The observation of a downward distortion of the paleoshorelines near the center of Siling Tso and Zhari Nam Tso (Figure 2) thus suggests a long enough relaxation time that it allows the surface to continue subsiding after the lake started regressing.

5.3 Reconciliation of results inferred from decadal and millennial time scales

The analysis of Doin *et al*., 2015 and our own modeling results (Figure 6) suggest an equivalent elastic thickness *Te* ~30 km at decadal time scale larger than our estimate of *Te* <5-10 km derived at the millennial time scale from the paleoshorelines (Figures 5 and 6 and Supplementary Figure E.2). We also find that, at the decadal time scale, a viscosity of ~10^{18} Pa.s lower than at the millennial time scale. The domains of acceptable model parameters do not overlap (Figures 5 and 6a relative to 6b). The effective rheology of the Tibetan crust, when represented by an elastic lid over a finite viscoelastic medium thus appears time-dependent. This behavior could reflect that the effective viscosity is actually time-dependent as could happen for example with a non-linear (stress-dependent) rheology or a Burgers body rheology. A Burgers body, which consists of a Maxwell element in series with a Kelvin element, is a common model used in postseismic studies (*e.g*., Burgman & Dresen, 2005). Such a model has a short-term viscosity, associated to the Kelvin element, and a long-term viscosity associated to the Maxwell element. A

501 depth-varying viscosity would also imply a time-dependent effective viscosity in
502 response to a surface load. We therefore test if these alternative models can reconcile the
503 results obtained at the decadal and millennial time-scale. In these calculations we use the
504 modeling approach of Bills *et al*., 1994, which allows different short-term and long-term
505 viscosities and depth variations.
506
507 We produce synthetic data at the decadal and millennial time scale with simplified
508 loading history similar to the ones assumed in the actual data analysis. We next invert the
509 synthetic data using the same inversion procedure as above. A cylindrical load of 50 km
510 in radius and a height of 140 m, 60 m and 10 m were chosen to represent the lake load for
511 the millennial (Zhari Nam Tso "long-term" and Siling Tso "mid-term") and decadal
512 (Siling Tso "short-term") cases respectively. We assume two long-term load histories. A
513 'long term' one is similar to that inferred at Zhari Nam Tso: the load corresponding to the
514 highstand is applied from 12 ka to 8 ka and removed afterwards. The "mid-term" one
515 corresponds to Siling Tso: the load is applied from 10 ka to 4 ka and removed afterwards.
516 At the decadal timescale we assume 10 m of transgression over 10 years, which is similar
517 to the Siling Tso case (Doin *et al*., 2015). For a given viscosity profile, we generate three
518 synthetic datasets representing the three time scales, which are then inverted to find the
519 best equivalent simple viscoelastic model, consisting of an elastic lid over a viscous
520 channel as assumed above. We test a Burgers body model (Figures 9). In that case two
521 Maxwell elements in parallel are used to produce an equivalent Burgers body rheology
522 (Muller, 1986). We also test a multilayered model (Figures 10).
523

524 The model of Figure 9 contains a 60 km thick viscoelastic layer with a transient viscosity
525 of 10^{18} Pa.s and a steady state viscosity of 10^{20} Pa.s. The multilayered model of Figure
526 10, assumes a Maxwell rheology in each layer. The model assumes lower viscosity at
527 mid-crustal depth where the temperature has presumably a local maximum due to the
528 temperature inversion caused by the underthrusting of India beneath Tibet (*e.g.*, Wang *et*
529 *al*., 2013). The inversion of the synthetic data generated with both models yield low
530 elastic thicknesses at the millennial timescales and higher elastic thicknesses at the
531 decadal cases. This is particularly clear for the stratified model (Figure 10). At both
532 "long-term" and "mid-term" timescales the equivalent elastic thicknesses is <10 km
533 whereas for a "short-term" decadal timescale the equivalent elastic thickness is >20 km.
534 The apparent viscosities vary significantly. Compared to the "long term" case, it is lower
535 by a factor 2 in the "mid-term" and by a factor 10 in the "short term" (Figure 10). These
536 trends are similar to those observed in the inversion of the Siling Tso and Zhari Nam Tso
537 data. We note that the inversion of synthetic data generated with the stratified model
538 reproduces better the trade-off between η, *Te* and *L* at the decadal and millennial time
539 scales.
540

541 ## 6 Conclusion

542 We used the deformation response to lake level variations at the decadal and millennial
543 time scale to place constraints on the rheology of the Tibetan crust. Our study confirms
544 and expands the results of the previous studies presented by England *et al*., 2013, Shi *et*
545 *al*., 2015 and Doin *et al*., 2015. Compared to the Lake Bonneville archetype (Bills &
546 May, 1987; Nakiboglu & Lambeck, 1982), the paleoshorelines around the Tibetan lakes

studied here show much smaller distortions, despite a comparable lake regression, and a downward deflection of the centers of the lakes instead of an upward deflection. The downward deflection is a signature of channel flow in the crust, but the upper crust must have remained well coupled, at the millennial time scale, to a quasi-rigid sub-crustal lid to explain the small distortion of the shorelines. Reconciling the millennial and decadal deformation response can be achieved with either vertical layering or a non-linear rheology. For example, a Burgers body rheology with a transient viscosity of 10^{18} Pa.s and a long term viscosity of 10^{20} Pa.s could reproduce the deformation response at both the decadal and the millennial time scale. An example of an alternatively layered model has a lower viscosity (10^{18} Pa.s) mid-crust (between ~10 and 30 km depth) embedded in a higher viscosity crust (>10^{20} Pa.s). A viscosity <10^{18} Pa.s, as proposed in some studies, could only exist in a thin layer (<10 km). The crustal rheology derived from this study is consistent with the low effective elastic thickness of Tibet, *Te* ~8 km, derived from gravity studies (Braitenberg *et al*., 2003). Indeed the short-wavelength deformation of the paleoshorelines requires a small *Te* (<5 km) of the upper-crustal lid and some degree of relaxation through mid-crustal channel flow at the millennial time scale. Only the thin upper crustal lid would be able to support topographic loads at the much longer geological time scale associated with the evolution of topography.

Acknowledgements: This study was partially supported by NSF award EAR-1821853. We thank Marie-Pierre Doin for providing the data used for the analysis of the ground deformation driven by modern water level variations of Siling Tso. We also thank one

570 anonymous reviewer and Philip England for insightful comments that considerably help
571 improve this contribution.

572

573 ## References

574 Ahlborn, M., Haberzettl, T., Wang, J., Fürstenberg, S., Mäusbacher, R., Mazzocco, J.,
575 Pierson, J., Zhu, L. & Frenzel, P. (2016). Holocene lake level history of the Tangra Yum
576 Co lake system, southern-central Tibetan plateau. *The Holocene 26* (2), 176–187.

577

578 Avouac, J.-P., Dobremez, J.-F. & Bourjot, L. (1996). Palaeoclimatic interpretation of a
579 topographic profile across middle holocene regressive shorelines of Longmu Co (western
580 Tibet). *Palaeogeography, Palaeoclimatology, Palaeoecology 120*(1-2), 93– 104.

581

582 Beaumont, C., Jamieson, R. a., Nguyen, M. H. & Lee, B. (2001). Himalayan tectonics
583 explained by extrusion of a low-viscosity crustal channel coupled to focused surface
584 denudation. *Nature 414*(6865), 738–742.

585

586 Bills, B. G., Currey, R. & Marshall, G. A. (1994). Viscosity estimates for the crust and
587 upper mantle from patterns of lacustrine shoreline deformation in the Eastern Great
588 Basin. *Journal of Geophysical Research 99086*(10), 59–22.

589

590 Bills, B. G. & May, G. M. (1987). Lake Bonneville: Constraints on Lithospheric
591 Thickness and Upper Mantle Viscosity From Isostatic Warping of Bonneville, Provo, and
592 Gilbert Stage Shorelines. *Journal of Geophysical Research-Solid Earth and Planets*
593 *92*(B11), 11493–11508.

594

595 Bills, B.G., K.D. Adams, S.G. Wesnousky (2007), Viscosity structure of the crust and
596 upper mantle in western Nevada from isostatic rebound patterns of the late Pleistocene
597 Lake Lahontan high shoreline, *Journal of Geophysical Research* B06405,112.

598

599 Braitenberg, C., Wang, Y., Fang, J. & Hsu, H. (2003). Spatial variations of flexure
600 parameters over the Tibet–Quinghai plateau. *Earth and Planetary Science Letters 205*(3),
601 211–224.

602

603 Brotchie, J. & Silvester, R. (1969). On crustal flexure. *Journal of Geophysical Research*
604 *74*(22), 5240–5252.

605

606 Bürgmann, R. & Dresen, G. (2008). Rheology of the lower crust and upper mantle:
607 Evidence from rock mechanics, geodesy, and field observations. *Annual Review of Earth*
608 *and Planetary Sciences*, **36**, 531–567.

609

610 Burov, E., Watts, T., Podladchikov, Y. & Evans, B. (2014). Observational and modeling
611 perspectives on the mechanical properties of the lithosphere. *Tectonophysics*, **631**, 1–3.

612

613 Chen, Y., Zong, Y., Li, B., Li, S. & Aitchison, J. C. (2013). Shrinking lakes in Tibet
614 linked to the weakening asian monsoon in the past 8.2 ka. *Quaternary Research 80*(2),
615 189–198.

616

617 Clark, M. K., Bush, J. W. M. & Royden, L. H. (2005). Dynamic topography produced by
618 lower crustal flow against rheological strength heterogeneities bordering the Tibetan
619 Plateau. *Geophysical Journal International 162*(2), 575–590.

620

621 Clark, M. K. & Royden, L. H. (2000). Topographic ooze: Building the eastern margin of
622 Tibet by lower crustal flow. *Geology 28*(8), 703–706.

623

624 Copley, A., Avouac, J.-P. & Wernicke, B. P. (2011). Evidence for mechanical coupling
625 and strong Indian lower crust beneath southern Tibet. *Nature 472*(7341), 79–81.

626

627 Doin, M. P., Twardzik, C., Ducret, G., Lasserre, C., Guillaso, S. & Jianbao, S. (2015).
628 InSAR measurement of the deformation around Siling Co Lake: Inferences on the lower

629 crust viscosity in central Tibet. *Journal of Geophysical Research: Solid Earth 120*(B7),
630 5290–5310.

631

632 England, P. C. & Walker, R. T. (2016). Comment on: "crustal strength in central Tibet
633 determined from holocene shoreline deflection around Siling Co" by Xuhua Shi, Eric
634 Kirby, Kevin P. Furlong, Kai Meng, Ruth Robinson and Erchie Wang. *Earth and*
635 *Planetary Science Letters*, **433**, 393–395.

636

637 England, P. C., Walker, R. T., Fu, B. & Floyd, M. A. (2013). A bound on the viscosity of
638 the Tibetan crust from the horizontality of palaeolake shorelines. *Earth and Planetary*
639 *Science Letters*, **375**, 44–56.

640

641 Gasse, F., Arnold, M. et al. (1991). A 13,000-year climate record from western Tibet.
642 *Nature 353*(6346), 742.

643

644 Hilley, G., Johnson, K., Wang, M., Shen, Z.-K. & Bürgmann, R. (2009). Earthquake-
645 cycle deformation and fault slip rates in northern Tibet. *Geology 37*(1), 31–34.

646

647 Hilley, G. E., Bürgmann, R., Zhang, P. Z. & Molnar, P. (2005). Bayesian inference of
648 plastosphere viscosities near the Kunlun Fault, northern Tibet. *Geophysical Research*
649 *Letters 32*(1), 1–4.

650

651 Huang, M.-H., Bürgmann, R. & Freed, A. M. (2014). Probing the lithospheric rheology
652 across the eastern margin of the Tibetan plateau. *Earth and Planetary Science Letters*,
653 396, 88–96.

654

655 Huc, M., Hassani, R. & Chéry, J. (1998). Large earthquake nucleation associated with
656 stress exchange between middle and upper crust. *Geophysical research letters 25* (4),
657 551–554.

658

659 Hudson, A. M., Quade, J., Huth, T. E., Lei, G., Cheng, H., Edwards, L. R., Olsen, J. W.
660 & Zhang, H. (2015). Lake level reconstruction for 12.8–2.3 ka of the ngangla ring tso
661 closed-basin lake system, southwest Tibetan plateau. *Quaternary Research 83*(1), 66–79.

662

663 Jackson, J. (2002). Strength of the continental lithosphere: time to abandon the jelly
664 sandwich? *GSA Today 12*(9), 4–9.

665

666 Johnson, K. & Segall, P. (2004). Viscoelastic earthquake cycle models with deep stress-
667 driven creep along the san andreas fault system. *Journal of Geophysical Research: Solid*
668 *Earth 109*(B10).

669

670 Kaufman, G. & Amelung, F. (2000). Reservoir-induced deformacion and continental
671 rheology in vicinity of lake mead. *Journal of Geophysical Research 105*(B7), 341– 358.

672

673 Kessler, M. A., Anderson, R. S. & Stock, G. M. (2006). Modeling topographic and
674 climatic control of east-west asymmetry in sierra nevada glacier length during the last
675 glacial maximum. *Journal of Geophysical Research: Earth Surface 111*(F2).

676

677 Klemperer, S. L. (2006). Crustal flow in Tibet: geophysical evidence for the physical
678 state of Tibetan lithosphere, and inferred patterns of active flow. *Geological Society,*
679 *London, Special Publications 268*(1), 39–70.

680

681 Kong, P., Na, C., Brown, R., Fabel, D., Freeman, S., Xiao, W. & Wang, Y. (2011).
682 Cosmogenic 10be and 26al dating of paleolake shorelines in Tibet. *Journal of Asian*
683 *Earth Sciences 41*(3), 263–273.

684

685 Lee, J., Li, S.-H. & Aitchison, J. (2009). Osl dating of paleoshorelines at Lagkor Tso,
686 western Tibet. *Quaternary Geochronology 4*(4), 335–343.

687

688 León Soto, G., Sandvol, E., Ni, J. F., Flesch, L., Hearn, T. M., Tilmann, F., Chen, J. &
689 Brown, L. D. (2012). Significant and vertically coherent seismic anisotropy beneath
690 eastern Tibet. *Journal of Geophysical Research: Solid Earth 117*(5).

691

692 Masek, J. G., Isacks, B. L., Fielding, E. J. & Browaeys, J. (1994). Rift flank uplift in
693 Tibet: Evidence for a viscous lower crust. *Tectonics 13*(3), 659–667.

694

695 Nakiboglu, S. & Lambeck, K. (1982). A study of the Earth's response to surface loading
696 with application to lake Bonneville. *Geophysical Journal International 70*(3), 577– 620.

697

698 Neal, R. M. (2003). Slice sampling. *Annals of statistics*, 705–741.

699

700 Nelson, K. D., Zhao, W., Brown, L. D., Kuo, J., Che, J., Liu, X., Klemperer, S. L.,
701 Makovsky, Y., Meissner, R., Mechie, J., Kind, R., Wenzel, F., Ni, J., Nabelek, J., Leshou,
702 C., Tan, H., Wei, W., Jones, a. G., Booker, J., Unsworth, M., Kidd, W. S. F., Hauck, M.,
703 Alsdorf, D., Ross, a., Cogan, M., Wu, C., Sandvol, E. & Edwards, M. (1996). Partially

704 Molten Middle Crust Beneath Southern Tibet: Synthesis of Project INDEPTH Results.
705 *Science 274*(5293), 1684–1688.

706

707 Owen, L. A. & Dortch, J. M. (2014). Nature and timing of quaternary glaciation in the
708 Himalayan–Tibetan orogen. *Quaternary Science Reviews*, **88**, 14–54.

709

710 Müller, G. (1986). Generalized Maxwell bodies and estimates of mantle viscosity.
711 *Geophysical Journal of the Royal Astronomical Society*, *87*(3), 1113-1141.

712

713 Rades, E. F., Tsukamoto, S., Frechen, M., Xu, Q. & Ding, L. (2015). A lake-level
714 chronology based on feldspar luminescence dating of beach ridges at Tangra Yum Co
715 (southern Tibet). *Quaternary Research 83*(3), 469–478.

716

717 Royden, L. H., Burchfiel, B. C., King, R. W., Wang, E., Chen, Z., Shen, F. & Liu, Y.
718 (1997). Surface Deformation and Lower Crustal Flow in Eastern Tibet. *Science*
719 *276*(5313), 788–790.

720

721 Ryder, I., Bürgmann, R., & Pollitz, F. (2011). Lower crustal relaxation beneath the
722 Tibetan Plateau and Qaidam Basin following the 2001 Kokoxili earthquake. *Geophysical*
723 *Journal International*, *187*(2), 613-630.

724

725 Ryder, I., Wang, H., Bie, L., & Rietbrock, A. (2014). Geodetic imaging of late
726 postseismic lower crustal flow in Tibet. *Earth and Planetary Science Letters*, *404*, 136-
727 143.

728

729 Shi, X., Kirby, E., Furlong, K. P., Meng, K., Robinson, R. & Wang, E. (2015). Crustal
730 strength in central Tibet determined from Holocene shoreline deflection around Siling
731 Co. *Earth and Planetary Science Letters 423*(January), 145–154.

732

733 Shi, X., Kirby, E., Furlong, K. P., Meng, K., Robinson, R., Lu, H., & Wang, E. (2017).
734 Rapid and punctuated Late Holocene recession of Siling Co, central Tibet. *Quaternary*
735 *Science Reviews*, *172*, 15-31.

736

737 Unsworth, M., Wenbo, W., Jones, A. G., Li, S., Bedrosian, P., Booker, J., Sheng, J.,
738 Ming, D. & Handong, T. (2004). Crustal and upper mantle structure of northern Tibet
739 imaged with magnetotelluric data. *Journal of Geophysical Research: Solid Earth 109*
740 (B2).

741

742 Wang, C.-Y., Chen, W.-P. & Wang, L.-P. (2013). Temperature beneath Tibet. *Earth and*
743 *Planetary Science Letters*, **375**, 326–337.

744

745 Yamasaki, T. & Houseman, G. A. (2012). The crustal viscosity gradient measured from
746 post-seismic deformation: A case study of the 1997 Manyi (Tibet) earthquake. *Earth and*
747 *Planetary Science Letters*, **351-352**, 105–114.

748

749 Zhang, C. J., Cao, J. L. & Shi, Y. L. (2009). Studying the viscosity of lower crust of
750 Qinghai-Tibet Plateau according to post-seismic deformation. *Science in China, Series D:*
751 *Earth Sciences 52*(3), 411–419.

752

753 Zhao, W.-L. & Morgan, W. J. (1987). Injection of Indian crust into Tibetan lower crust:
754 A two-dimensional finite element model study. *Tectonics 6*(4), 489–504.

FIGURES

Figure 1: (a) Location of lakes discussed in this study. The estimated extent of Ngangla Ring Tso (NR), Taro Tso (T), Zhari Nam Tso (ZN), and Tangra Yum Tso (TY) is represented at the time of their early Holocene highstand and the Siling Tso (S) is represented at the time of its mid-Holocene highstand. (b) Satellite view (ESRI World Imagery; location: 86.17°E-31.07°N) showing well preserved shorelines marking the Holocene highstand of Zhari Nam Tso (white arrows). The sequence of paleoshorelines at lower elevation recorded the regression of the lake from the mid-Holocene to its present level. (c) Estimated lake level variation of Ngangla Ring Tso (Hudson *et al.*, 2015), Taro Tso (Lee *et al.*, 2009), Zhari Nam Tso (Chen *et al.*, 2013), and Tangra Yum Tso (Ahlborn *et al.*, 2016; Rades *et al.*, 2015) for the last 25 ky. Each curve is normalized to the highest stand. The highest stand is 4864 m at Ngangla Ring Tso (which is 83 m above the present lake level), 4606 m at Taro Tso (177 m above the present lake level), 4751 m at Zhari Nam Tso (134 m above the present lake level) and 4741 m at Tangra Yum Tso (201 m above the present lake level). Dashed lines show highly uncertain extrapolations. Lower panel shows simplified normalized lake level variation assumed in this study (red) and in England *et al.*, 2013 (orange). The double arrows represent the tested range of age at which the lakes initially reached their highstand. (d) Normalized water level variations of Siling Tso (Shi *et al.*, 2017 and references therein) and simplified normalized Siling Tso level variations considered in this study (green curve in lower panel). The highest stand is 4597 m at Siling Tso (which is 66 m above the present lake level).

Figure 2: Observed (color-coded circles) and modeled elevation at present of the paleoshorelines marking the Holocene highstand around Siling Tso (a) and Zhari Nam Tso (b). The color scale is centered on their mean restored elevation. The models assume an elastic lid overlying a viscoelastic channel with a rigid base. We selected models representative of the best fitting solutions. For Siling Tso, the elastic lid thickness is Te = 2 km, the viscoelastic channel is L = 9

km thick and the viscosity is $\eta = 1.8 \times 10^{18}$ Pa.s. For Zhari Nam Tso the elastic lid thickness is *Te* = 6.4 km, the viscoelastic channel is L = 5.9 km thick and the viscosity $\eta = 5 \times 10^{19}$ Pa.s. The model prediction for Zhari Nam Tso, takes into account the deformation associated to the surrounding lakes (Ngangla Ring Tso, Taro Tso and Tangra Yum Tso). The model prediction for the whole region including the 4 lakes is represented in Figure 4d. The data indicate deformation of small amplitude at a wavelength of about 100 km. Note also the counterintuitive observation of subsidence nearer the paleolake centers, which is most obvious for Siling Tso. The models are able to produce small amplitude deformation at a wavelength consistent with the observations as well as subsidence nearer the paleolake centers. Comparison between predicted and observed elevations are shown in Supplementary figure E1.

Figure 3:

Histograms of Siling Tso (a) and Zhari Nam Tso (b) highstand shoreline elevations and characterization of the wavelength of the post-highstand deformation of the paleoshorelines around Siling Tso (c) and Zhari Nam Tso (d). The histograms show the distribution of elevations of the raw data (green) and the filtered data (blue) obtained by averaging within a 10 km x 10 km sliding-window. The histogram of the differences between the filtered and unfiltered data (red) is the one considered to characterize the uncertainties on the paleoshoreline elevation for Siling Tso (standard deviation ~1.5 m) and Zhari Nam Tso (standard deviation ~1.4 m). The lower plots show the normalised standard deviation calculated within a sliding square window of 0 to 100 km width, of the post-highstand elevation change derived from the paleoshorelines elevation (black symbols). The data were filtered by averaging within a 10 km wide sliding-window to remove high frequency noise. This filtering helps comparison with the model predictions which have no noise. Error bars show the uncertainty on the calculated standard deviation at the 68% confidence level (1-σ). Windows with less than 20 data (chosen arbitrary to avoid poorly constrained values) were discarded. The standard deviation increases rapidly with the window

size and levels off for a window size exceeding ~60 km. This pattern indicates that the deformation signal has a wavelength of the order of 60 km. Prediction from one of the best models is shown for both Siling Tso and Zhari Nam Tso (Model 1, same as Figure 2). Model 2 corresponds to an elastic model with an elastic thickness *Te* = 10 km over an inviscid medium at the lower end of the elastic models of England *et al*., 2013. Model 3 corresponds to a model with the best set of parameters determined by Doin *et al.,* 2015; an elastic lid of thickness *Te* = 30 km overlying a viscoelastic channel of viscosity $\eta = 2x10^{18}$ Pa.s and thickness *L* = 35 km over a rigid base. The wavelength associated with models 2 and 3 is much larger than 60 km, as a result the standard deviation increases nearly linearly with the window size over the range of tested values contrary to what the data show.

Figure 4: Ground displacement around Ngangla Ring Tso, Taro Tso, Zhari Nam Tso and Tangra Yum Tso since their early Holocene highstand. (a) Range of calculated vertical displacements at the locations of the measured palaeoshorelines around Zhari Nam Tso. The model assumes an elastic lid over an inviscid fluid. The elastic thicknesses *Te* is varied between 1 km and 40 km. The removed load is constituted of the paleolake water bodies only (black), or include the load due to mountain glaciers assuming either a lower-bound (blue), or an upper-bound (red) extent (see supplements for details). The green shading shows the ~6 m range observed in the measurements. (b) Output from a particular elastic model with an elastic lid of thickness *Te* = 10 km over an inviscid medium at the lower end of the elastic models of England *et al.*, 2013. (c) Viscoelastic model with the best set of parameters inferred by Doin *et al.,* 2015; an elastic lid of thickness *Te* = 30 km overlying a viscoelastic channel of viscosity $\eta = 2x10^{18}$ Pa.s and thickness *L* = 35 km over a rigid base. (d) One of the best-fitting viscoelastic models obtained in this study with an elastic lid of thickness *Te* = 6.4 km overlying a viscoelastic channel of viscosity $\eta = 5x10^{19}$ Pa.s and thickness *L* = 5.9 km over a rigid base. The restored mean elevation of the

highstand before the regression according to each model is 4740.5 m (b), 4747.7 m (c) and 4750.7 m (d).

Figure 5: Results of the inversion of the Zhari Nam Tso highstand paleoshoreline assuming an elastic lid over a viscoelastic channel with a rigid base. The load due to the surrounding lakes (Ngangla Ring Tso, Taro Tso and Tangra Yum Tso) is taken into account. The 2-dimensional slices into the 4 parameters inversion show the reduced chi-square, as defined in the text (Equation 1), as a function of the thickness and viscosity of the viscoelastic channel. The range of tested elastic thickness increases from left to right (0-10 km, 10-20 km and 20-30 km). From top to bottom the range of highstand duration increases: (a) 1.5 to 4.5 ky (highstand reached between 10-13 ka), (b) 4.5-8.5 ky (highstand reached between 13-17 ka) and (c) 8.5-11.5 ky (highstand reached between 17-20 ka).

Figure 6: (a) Results of the inversion of the highstand paleaoshoreline around Siling Tso assuming an elastic lid over a viscoelastic channel with a rigid base. (b) Results of the inversion of deformation response to the lake level rise of Siling Tso between 2000 and 2006 as predicted by the best-fitting model of Doin *et al.,* 2015. The model also assumes an elastic lid over a viscoelastic channel with a rigid base. The 2-dimensional slices into the 3 parameters inversion show the reduced chi-square (normalised for short-term analysis) as a function of the thickness L and viscosity η of the viscoelastic channel (up) or the elastic thickness Te and the viscosity η of the viscoelastic channel (down). The range of tested elastic thickness Te or channel thickness L increases from left to right (0-10 km, 10-20 km and 20-30 km).

Figure 7: Evaluation of the effect of subcrustal viscoelastic support. The models assume an elastic lid of thickness Te = 2 km overlying a 9 km thick viscoelastic channel with a viscosity η = 1.8×10^{18} Pa.s. The model in (a) assumes a rigid base (modeled with a Young modulus of 10^{20} Pa and a Poisson's ratio of 0.5) below the crustal viscous channel. The model (b) assumes a 35km

thick elastic layer overlying a viscoelastic half space with a viscosity of 10^{18} Pa.s. The mean restored elevation from model shown in (a) and (b) is 4596.8 m and 4594.7 m respectively. Map view (c) is the difference between models shown in (a) and (b). The difference shows low amplitude (<2m) long-wavelength (>100km) signal. The histogram (d) represents the differences of the restored elevations from model predictions shown in (a) and (b) at the location of the observed paleoshorelines. The histogram underlines the relatively low difference on elevation predictions (< 2m) between models with or without a rigid base.

Figure 8: Sketch illustrating the effect of viscous relaxation on the time evolution of surface displacements shown in Supplementary figure D1. The load is cylindrical and increases linearly from 16 ka to 12 ka before present. It reaches a maximum of 140 m of equivalent water thickness, stays constant from 12 ka to 8 ka and decreases linearly to 0 from 8 ka to present. The radius (R) of the load is 60 km. Surface displacements relative to the horizontal initial stage at 16 ka are calculated assuming an elastic lid with thickness of 6 km overlying a viscoelastic channel with thickness of 6 km and viscosity of $\eta = 10^{18}$ Pa.s, $\eta = 10^{19}$ Pa.s, or $\eta = 10^{20}$ Pa.s (from left to right respectively). (a) Surface vertical displacement along a radial cross section starting at the center of the cylindrical load calculated at 8 ka, 4 ka and at present. (b) Difference between the displacements at 8 ka and 4 ka (light blue) and between 8 ka and present (dark blue).

Figure 9: Synthetic test demonstrating how the apparent time dependent rheology deduced from the observations can result from a biviscous Burger rheology. We calculated the ground deformation due to a 100 km wide cylindrical time-varying load using the viscoelastic code from Bills *et al*., 1994. The model assumes a 5 km elastic lid over a 60 km thick viscoelastic layer with a transient viscosity of 10^{18} Pa.s (dashed line) and a long-term viscosity of 10^{20} Pa.s, overlying an elastic half space. Three synthetic datasets corresponding to either a long-term (~ Zhari Nam Tso), a mid-term (~ Siling Tso) or a short term (~ present-day Siling Tso) scenario were

produced. Two scenarios mimic the post Late Glacial Maximum history of lake transgression and regression observed at Zhari Nam Tso and Siling Tso. It assumes a highstand from 12 ka to 8 ka (similar to Zhari Nam Tso) or from 10 ka to 4 ka (similar to Siling Tso). The other loading history mimics the recent transgression of lake Siling Tso. It assumes a transgression of 10 m over 10 years (present-day Siling Tso). The synthetic displacements are then inverted using the same methodology as the one used to invert the real observations. Results of the inversion of the long-term (a), the mid-term (b) and the short-term (c) scenarios are shown as 2 dimensional slices into the 3 parameters space for different ranges of elastic thickness.

Figure 10: Synthetic test demonstrating how the apparent time-dependent rheology deduced from the observations can result from depth variations of viscosity. We calculated the ground deformation due to a 100 km wide cylindrical time-varying load using the viscoelastic code from Bills *et al*., 1994. The model assumes a 5km elastic lid over a 60 km thick stratified viscoelastic body overlying an elastic half-space. Crustal viscosities vary between 10^{18} Pa.s and 10^{21} Pa.s. The minimum viscosity is a mid-crustal depth where the temperature is presumably maximum (Wang *et al*., 2013). Three synthetic datasets corresponding to either a long-term (~ Zhari Nam Tso), a mid-term (~ Siling Tso) or a short term (~ present-day Siling Tso) scenario were produced as in Figure 9, and inverted using the same methodology as the one used to invert the real observations. Results of the inversion of the long-term (a), the mid-term (b) and the short-term (c) scenarios are shown as 2 dimensional slices into the 3 parameters space for different ranges of elastic thickness.

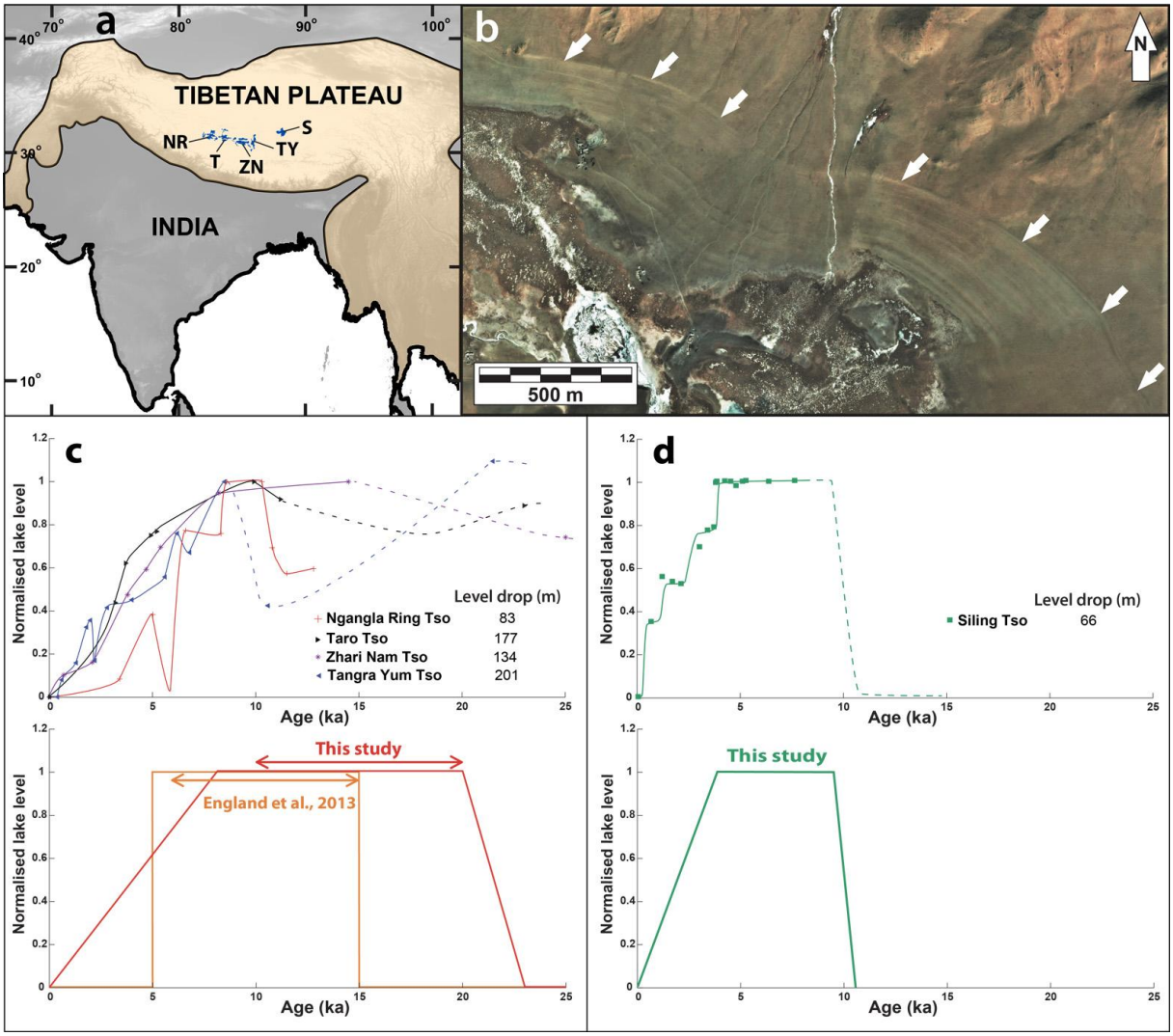
a
TIBETAN PLATEAU
INDIA
NR
S
TY
T
ZN
70°
80°
90°
100°
40°
30°
20°
10°
b
N
500 m
c
Normalised lake level
Age (ka)
Level drop (m)
Ngangla Ring Tso 83
Taro Tso 177
Zhari Nam Tso 134
Tangra Yum Tso 201
This study
England et al., 2013
d
Siling Tso 66
This study

Figure 1

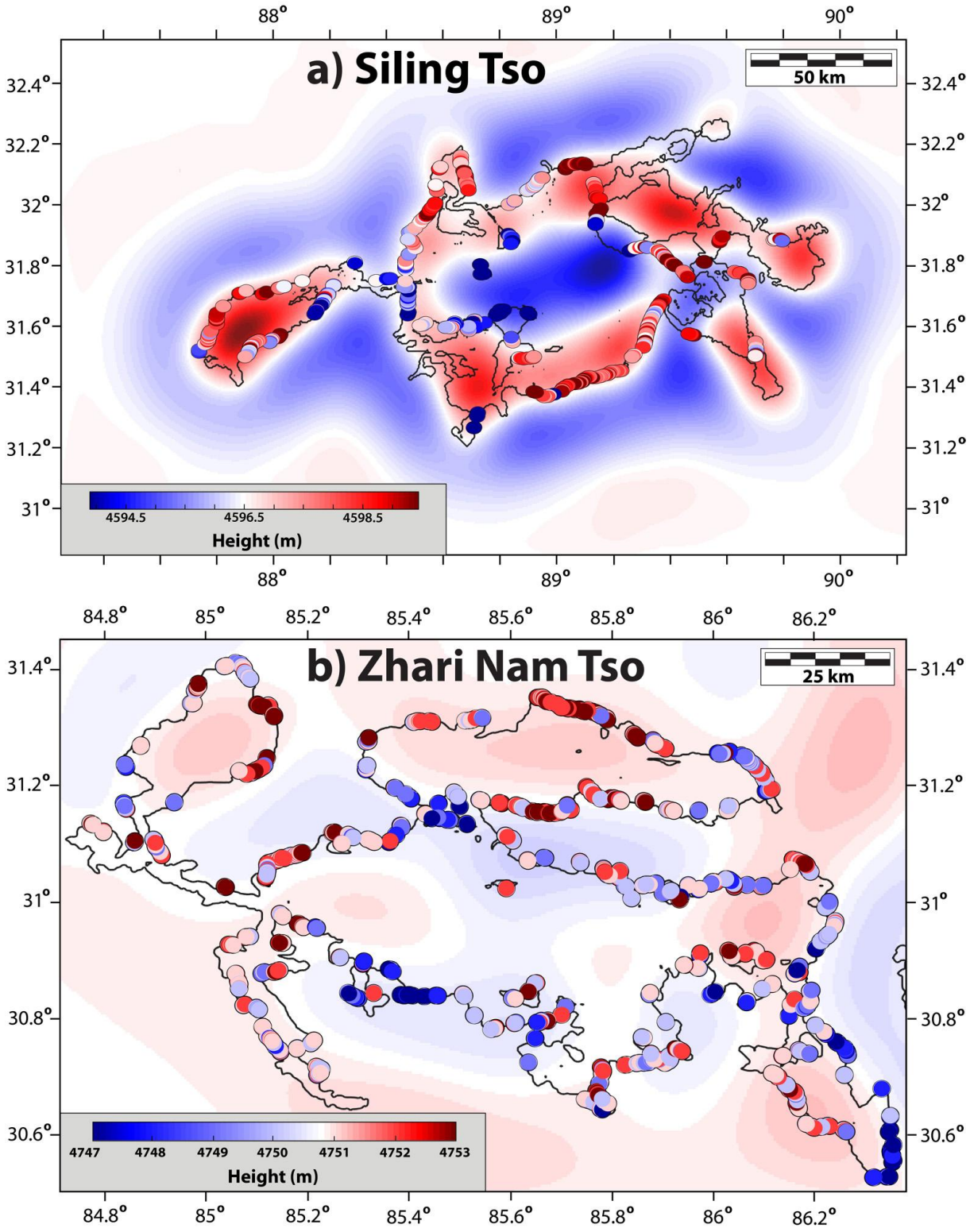
a) Siling Tso
50 km
88°
89°
90°
32.4°
32.2°
32°
31.8°
31.6°
31.4°
31.2°
31°
4594.5
4596.5
4598.5
Height (m)
b) Zhari Nam Tso
25 km
84.8°
85°
85.2°
85.4°
85.6°
85.8°
86°
86.2°
31.4°
31.2°
31°
30.8°
30.6°
4747
4748
4749
4750
4751
4752
4753
Height (m)

Figure 2

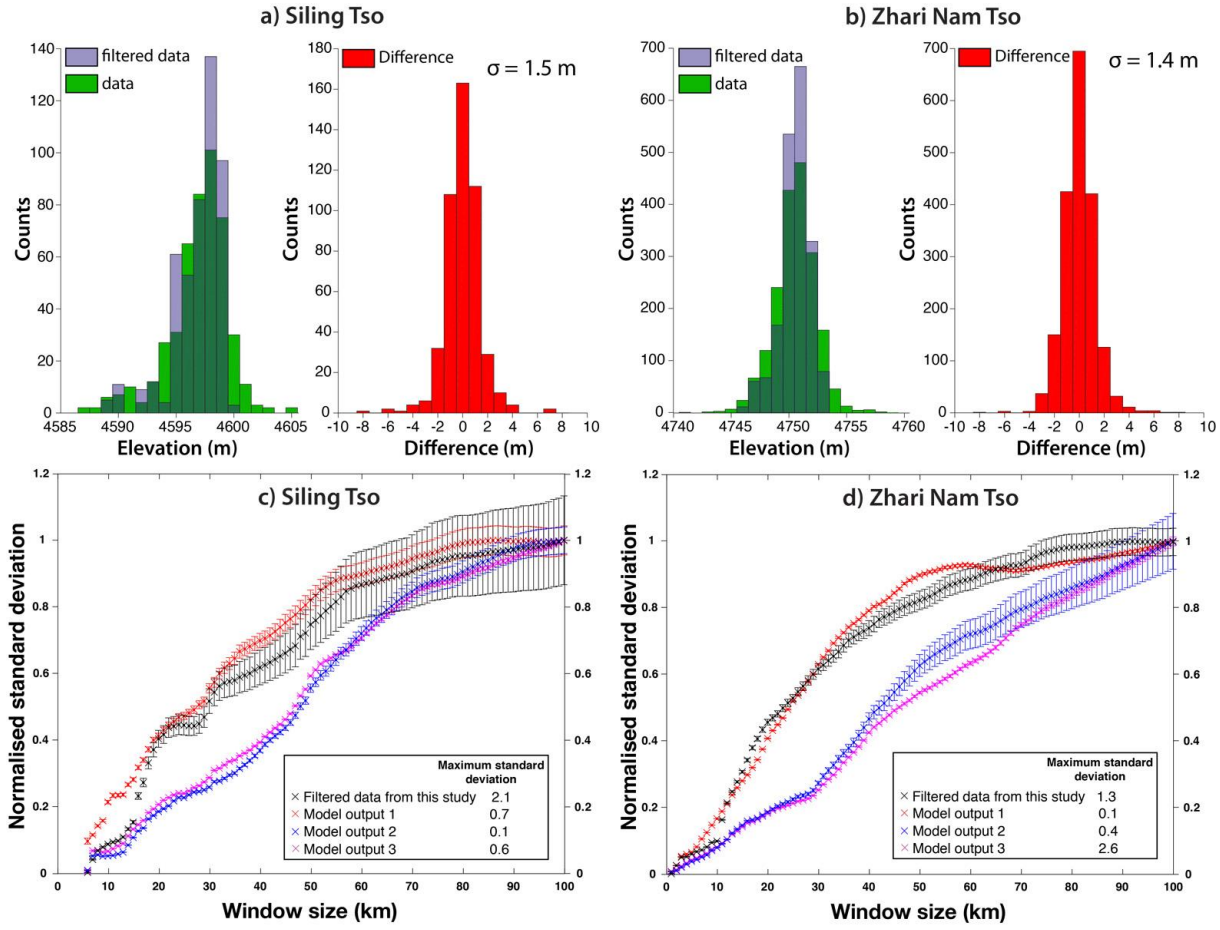

Figure 3

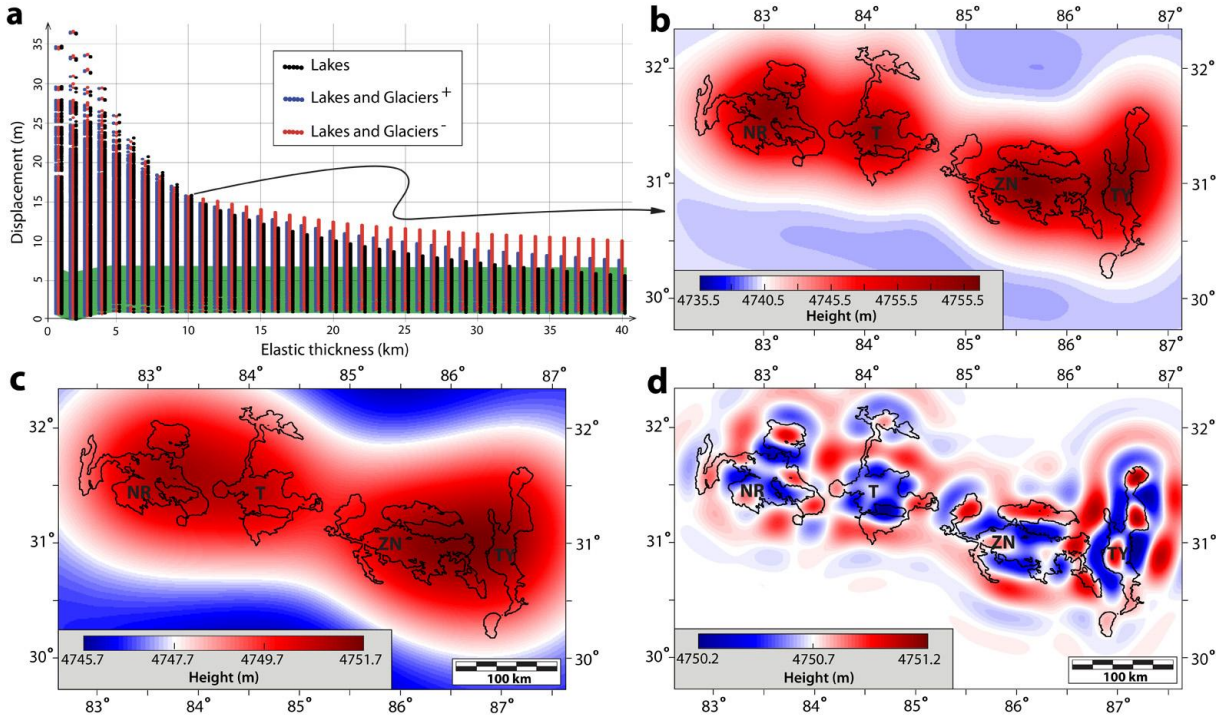

Figure 4

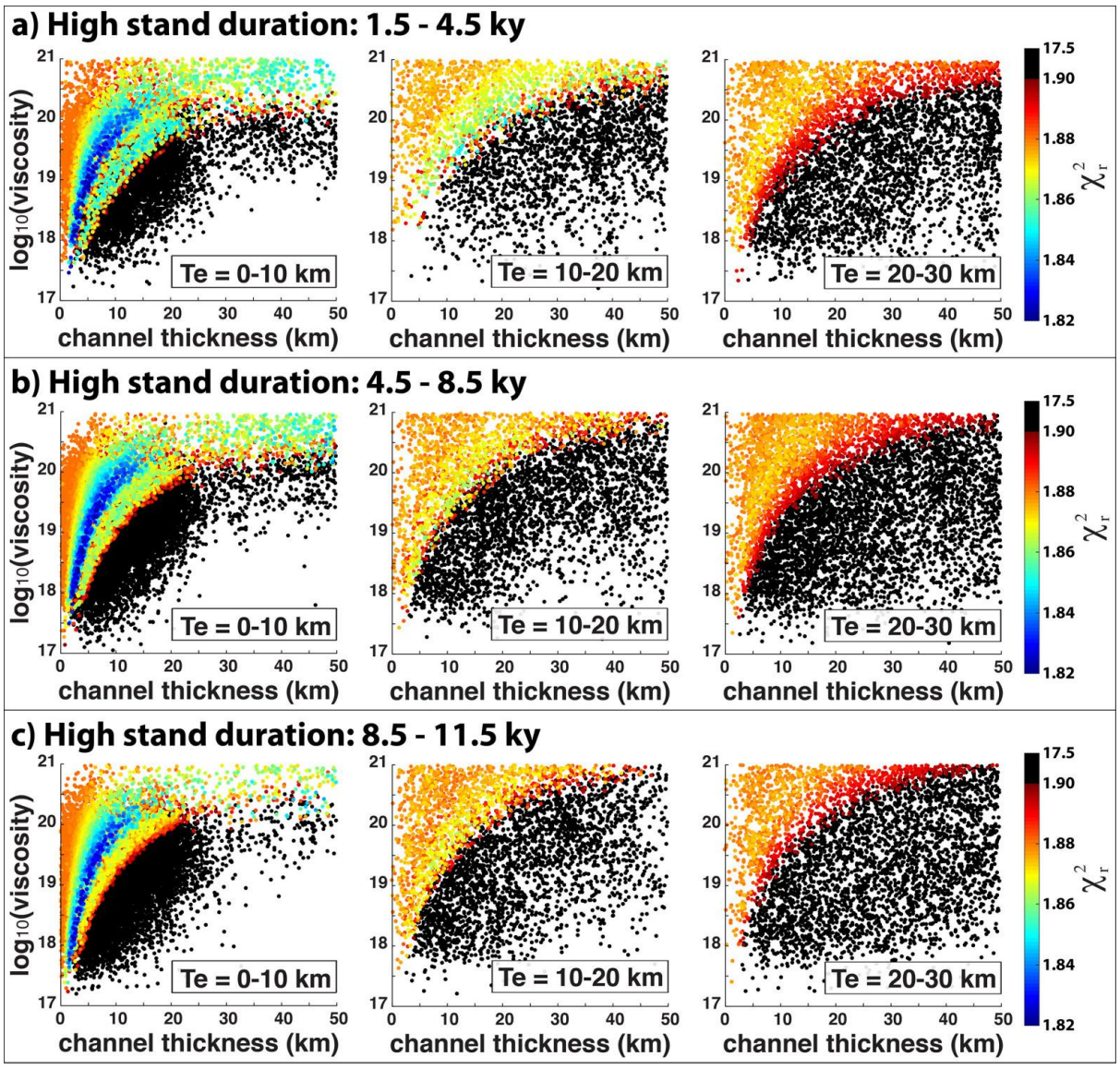
a) High stand duration: 1.5 - 4.5 ky
b) High stand duration: 4.5 - 8.5 ky
c) High stand duration: 8.5 - 11.5 ky
log10(viscosity)
channel thickness (km)
Te = 0-10 km
Te = 10-20 km
Te = 20-30 km
χ²r
17.5
1.90
1.88
1.86
1.84
1.82

Figure 5

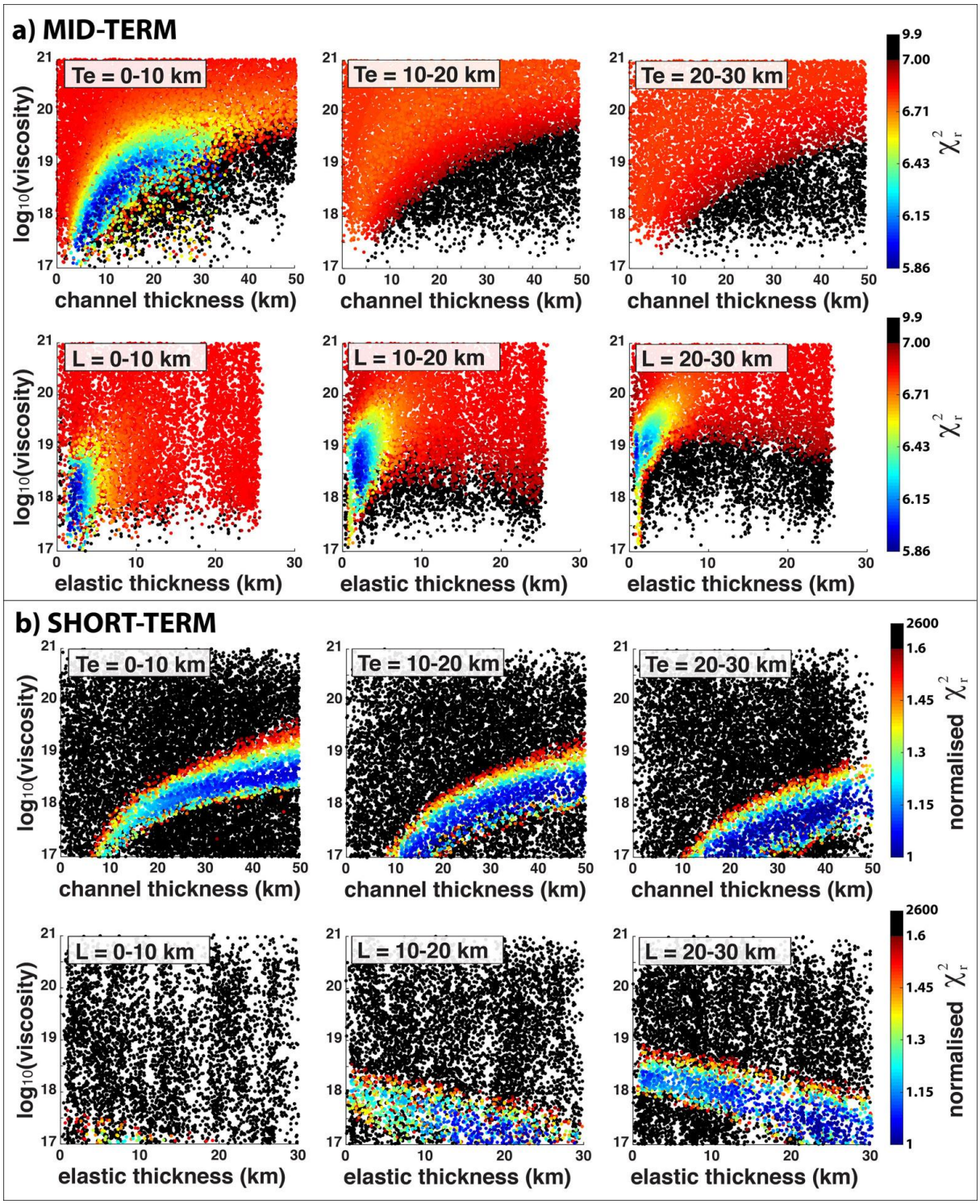
a) MID-TERM
Te = 0-10 km
Te = 10-20 km
Te = 20-30 km
L = 0-10 km
L = 10-20 km
L = 20-30 km
log10(viscosity)
channel thickness (km)
elastic thickness (km)
9.9
7.00
6.71
6.43
6.15
5.86
χ²r
b) SHORT-TERM
2600
1.6
1.45
1.3
1.15
1
normalised χ²r

Figure 6

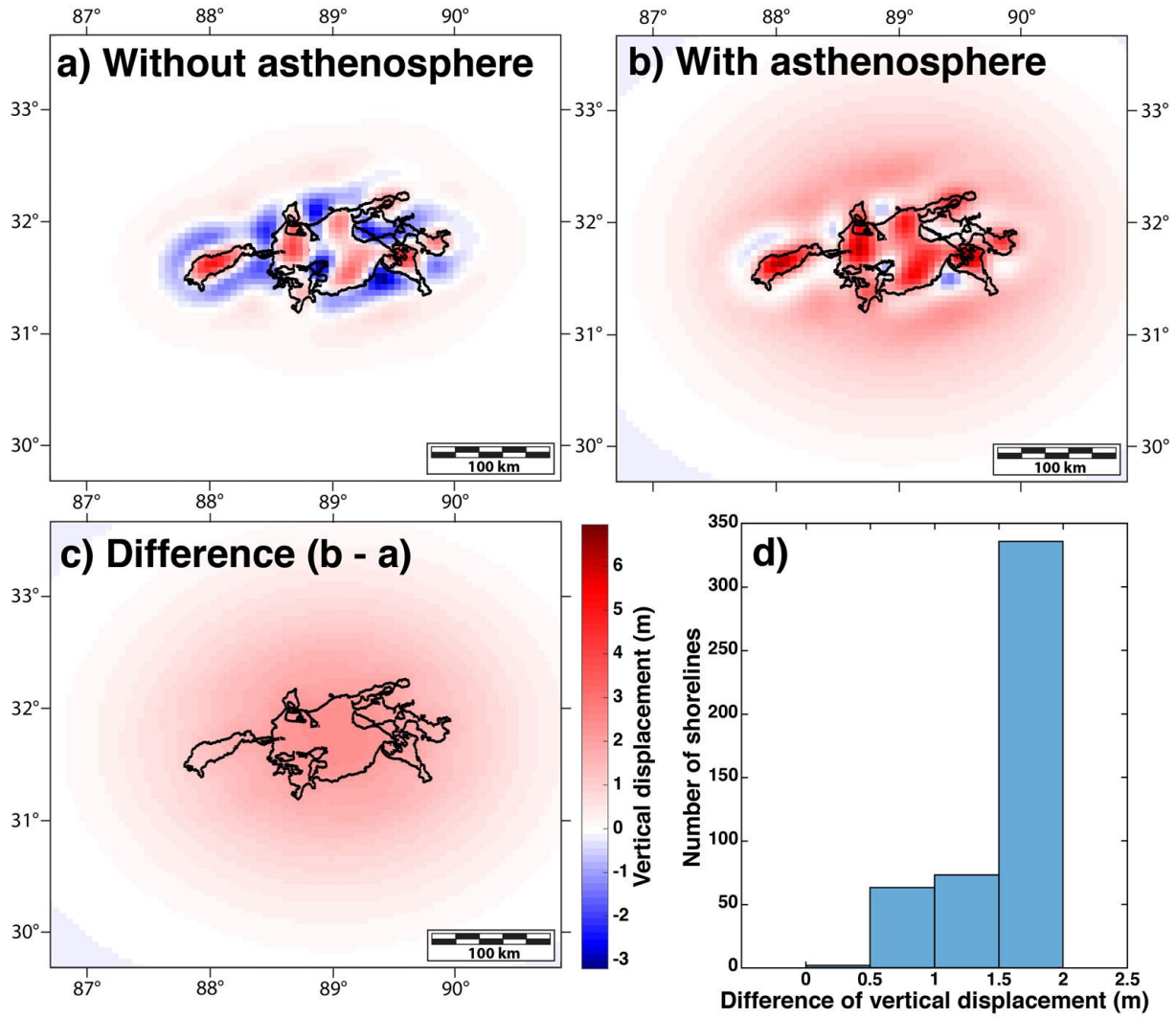
a) Without asthenosphere
b) With asthenosphere
c) Difference (b - a)
d)
87°
88°
89°
90°
33°
32°
31°
30°
100 km
Vertical displacement (m)
6
5
4
3
2
1
0
-1
-2
-3
Number of shorelines
350
300
250
200
150
100
50
0
0
0.5
1
1.5
2
2.5
Difference of vertical displacement (m)

Figure 7

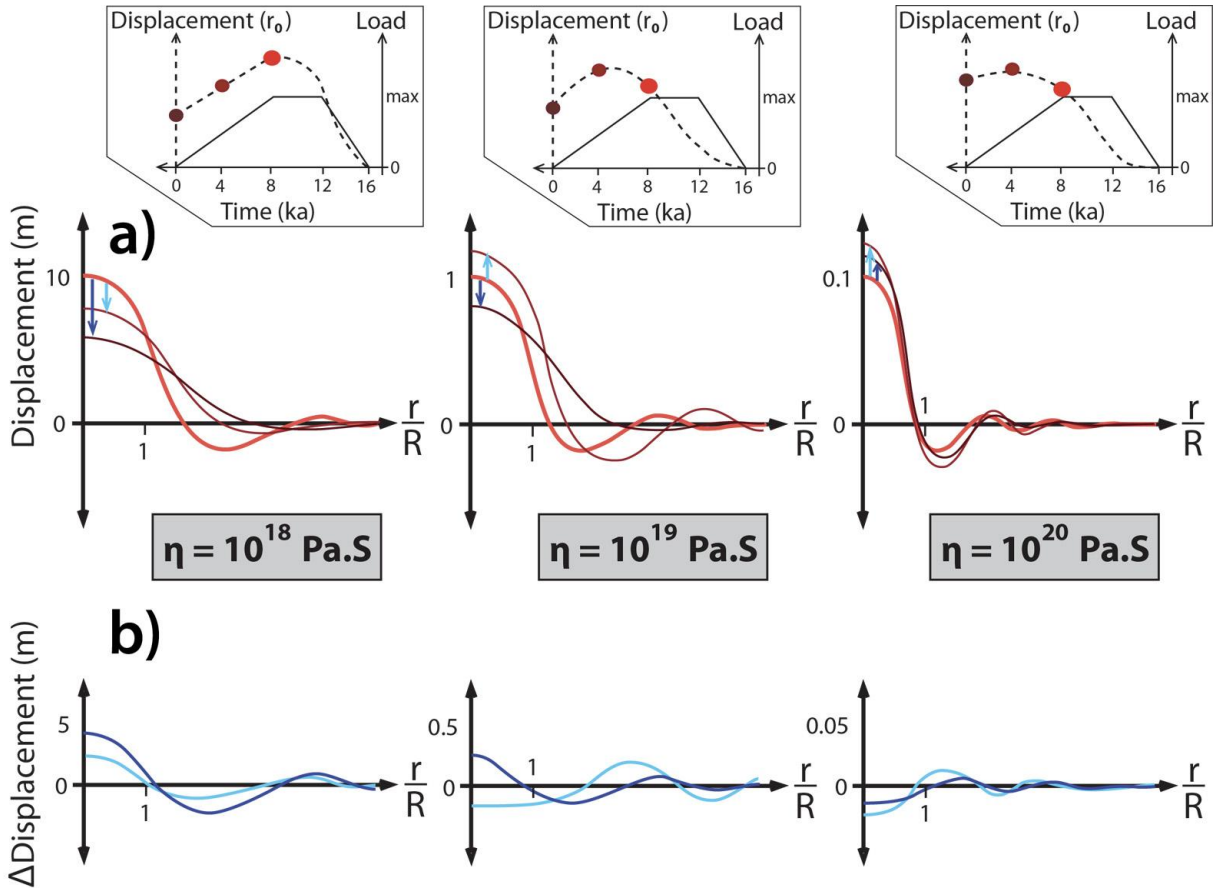
Displacement (r_0)
Load
max
0
0 4 8 12 16
Time (ka)
a)
Displacement (m)
10
1
0.1
r/R
η = 10^{18} Pa.S
η = 10^{19} Pa.S
η = 10^{20} Pa.S
b)
ΔDisplacement (m)
5
0.5
0.05

Figure 8

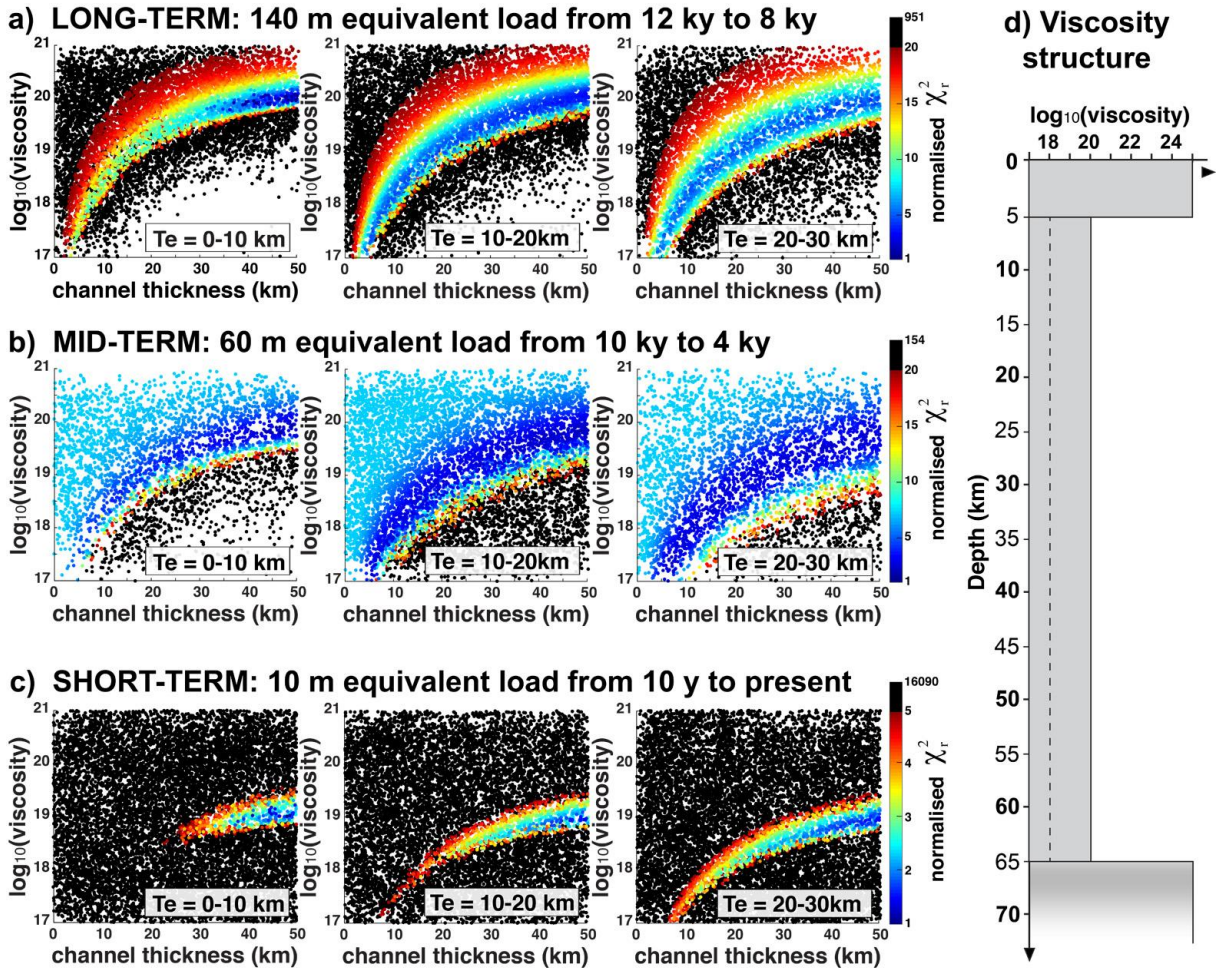
a) LONG-TERM: 140 m equivalent load from 12 ky to 8 ky
b) MID-TERM: 60 m equivalent load from 10 ky to 4 ky
c) SHORT-TERM: 10 m equivalent load from 10 y to present
Te = 0-10 km
Te = 10-20km
Te = 20-30 km
Te = 10-20 km
Te = 20-30km
log10(viscosity)
channel thickness (km)
normalised χ²r
951
154
16090
d) Viscosity structure
log10(viscosity)
Depth (km)

Figure 9

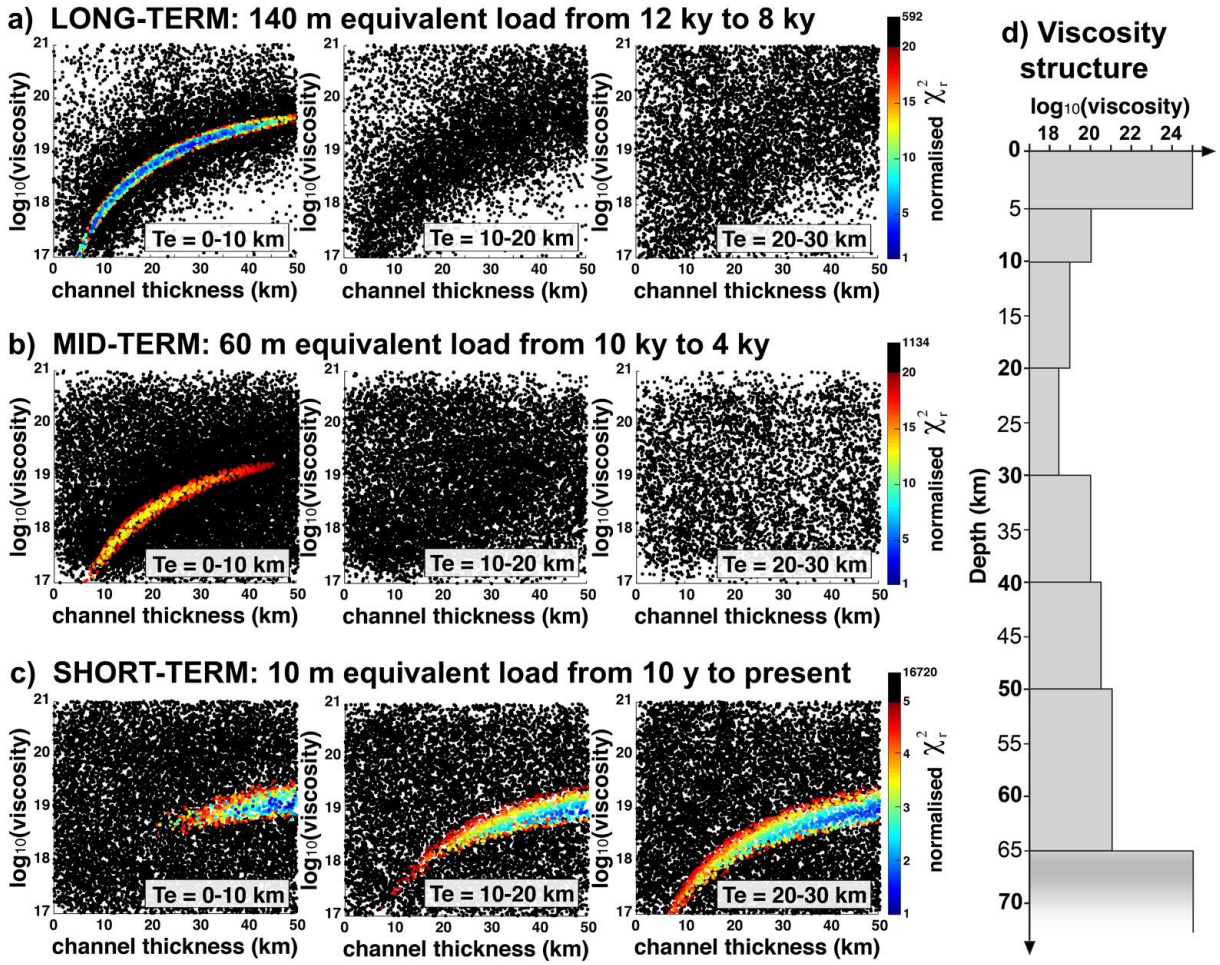
a) LONG-TERM: 140 m equivalent load from 12 ky to 8 ky
b) MID-TERM: 60 m equivalent load from 10 ky to 4 ky
c) SHORT-TERM: 10 m equivalent load from 10 y to present
Te = 0-10 km
Te = 10-20 km
Te = 20-30 km
log10(viscosity)
channel thickness (km)
normalised χ²r
592
1134
16720
d) Viscosity structure
log10(viscosity)
Depth (km)

Figure 10

SUPPLEMENTARY FIGURES

Figure A.1: Comparison between the SRTM-30m and AW3D30 Digital Elevation Models (DEMs) and the field measurements by England *et al.,* 2013 for paleoshorelines corresponding to the Holocene highstand around Zhari Nam Tso. The shaded topography (a and b) is centered on a region around Zhari Nam Tso where a paleoshoreline from the Holocene high stand has been sampled in 31 locations (center: 85.16°E, 31.07°N). (a) Topography from the ALOSWorld 3D global DEM of 30 m resolution (AW3D30) released in 2015 by the Japan Aerospace Exploration Agency (JAXA). (b) Shaded topography from the SRTM-30m global DEM (NASA JPL, 2014). (c) Elevations of 31 points (locations shown inset a and b and available in Supplementary files) extracted from AW3D30 (red) and SRTM-30m (blue) DEMs. The mean and standard deviation for each dataset is indicated in the legend. (d) Local slope vs differences between elevations of palaeoshorelines around Zhari Nam Tso measured using kinematic GPS by England *et al.,* 2013 and measured from the AW3D30 (red) and SRTM-30m DEM (blue). The mean and standard deviation for each dataset is indicated in the legend.

Figure A.2: Local slope and elevation from the AW3D30 DEM at the location of the measured highstand paleoshoreline around Zhari Nam Tso. From top to bottom the local slope is extracted from filtered DEM at 30 m, 60 m, 90 m and 150 m.

Figure A.3: Observed (color-coded circles) paleoshorelines marking the Holocene highstand around Siling Tso (a) and Zhari Nam Tso (b). The color scale is centered on their mean restored elevation as in Figure 2 (respectively 4596.5 m and 4750.7 m). The data indicate deformation of

small amplitude at a wavelength of about 100 km. Note also the counterintuitive observation of subsidence nearer the paleolake centers, which is most obvious for Siling Tso.

Figure B.1: Spatial distribution of the surface load changes due to the regression of paleolakes since their mid-Holocene highstand (NR: Ngangla Ring Tso; T: Taro Tso; ZN: Zhari Nam Tso; and TY: Tangra Yum Tso) and to the post Late Glacial Maximum retreat of the surrounding glaciers. The glaciers were reproduced using the Gc2d model Kessler *et al.,* 2006.

Figure D.1: Map views of the vertical ground displacement in response to a time-varying cylindrical load. In each plot the black circle represents the footprint of the 60 km wide cylindrical load. Displacement are measure relative to the surface elevation at the time of the end of the application of the load (chosen to 8 ka in these simulations), as it would have been recorded by the paleoshoreline marking a lake highstand. a: effects of a L = 6 km thick viscoelastic channel overlying a rigid base under a Te = 6 km thick elastic lid with a viscosity η of 10^{18} Pa.s, 10^{19} Pa.s and 10^{20} Pa.s. b: channel thickness effects of a viscoelastic channel with a viscosity $\eta = 10^{20.5}$ Pa.s underlying a Te = 6 km thick elastic lid with a thickness L of 6 km and 40 km. c: load history imposed in the simulations.

Figure E.1: Comparison between measured and predicted elevation (in meters) of the highstand paleoshoreline around Siling Tso (a) and Zhari Nam Tso relative to the initial elevation of the shoreline at the time the highstand, Z_0. Filtered elevations are from AW3D30 DEM (using a 10 km sliding window average filter). (a) Comparison with model predictions from the viscoelastic model of Figure 2 for Siling Tso. The parameters are: an elastic lid of Te = 2 km overlying a viscous channel of viscosity $\eta = 1.8\text{x}10^{18}$ Pa.s and thickness L = 9 km over a rigid base. The restored mean elevation (Zo) is 4596.5 m. (b) Comparison with model predictions from the viscoelastic model of Figure 2 for Zhari Nam Tso, taking into account the load associated to the surrounding lakes (Ngangla Ring Tso, Taro Tso and Tangra Yum Tso). The parameters are: an elastic lid of thickness

Te = 6.4 km overlying a viscous channel of viscosity $\eta = 5x10^{19}$ Pa.s and thickness *L* = 5.9 km over a rigid base. The restored mean elevation (Z_0) is 4750.7m.

Figure E.2: Constraints on the elastic thickness, *Te*, derived from the inversion of the deformation response to the lake level rise of Siling Co between 2000 and 2006 as predicted by the best-fitting model of Doin *et al.,* 2015, and from the inversion of the Zhari Nam Co and Siling Co high stand paleoshorelines (Figures 5 and 6). The models assume an elastic lid over a viscoelastic channel with a rigid base. We bin the tested models from *Te* =2 to 40 km with a 2 km interval. The mean of the 10 lowest reduced chi-squares is used to normalize the reduced chi-square for each set. Error bars show the standard deviation at the 68% confidence level (1-σ) of the mean of the 10 lowest reduced chi-squares in each bin. The best models from the inversion of Zhari Nam Tso (blue) and Siling Tso (red) highstand paleoshorelines have a low elastic thickness (< 10 km). The best models from the inversion of the deformation response to the lake level rise of Siling Tso between 2000 and 2006 (black) have larger elastic thicknesses of ~25 km.

Figure F.1: Deformation response to the lake level rise of Siling Tso between 2000 and 2006 predicted by the best-fitting model of Doin *et al*., 2015, used in this study as short-term "data". This viscoelastic model has an elastic lid of thickness *Te* = 30 km overlying a viscoelastic channel of viscosity $\eta = 2x10^{18}$ Pa.s and thickness *L* = 35 km over a rigid base.

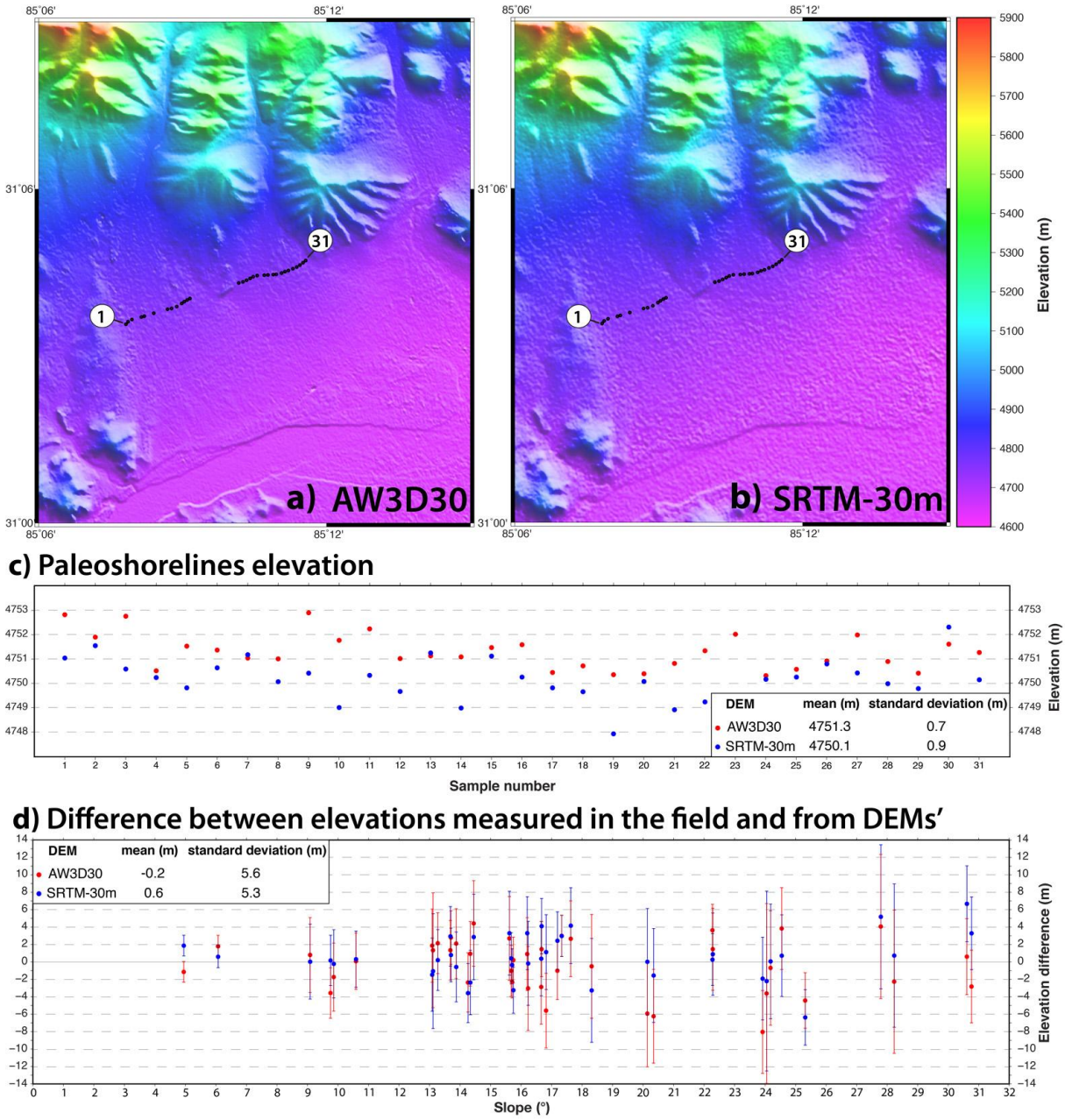
85°06'
85°12'
31°06'
31°00'
a) AW3D30
b) SRTM-30m
1
31
Elevation (m)
5900
5800
5700
5600
5500
5400
5300
5200
5100
5000
4900
4800
4700
4600
c) Paleoshorelines elevation
DEM mean (m) standard deviation (m)
AW3D30 4751.3 0.7
SRTM-30m 4750.1 0.9
Sample number
d) Difference between elevations measured in the field and from DEMs'
DEM mean (m) standard deviation (m)
AW3D30 -0.2 5.6
SRTM-30m 0.6 5.3
Elevation difference (m)
Slope (°)

Figure A.1

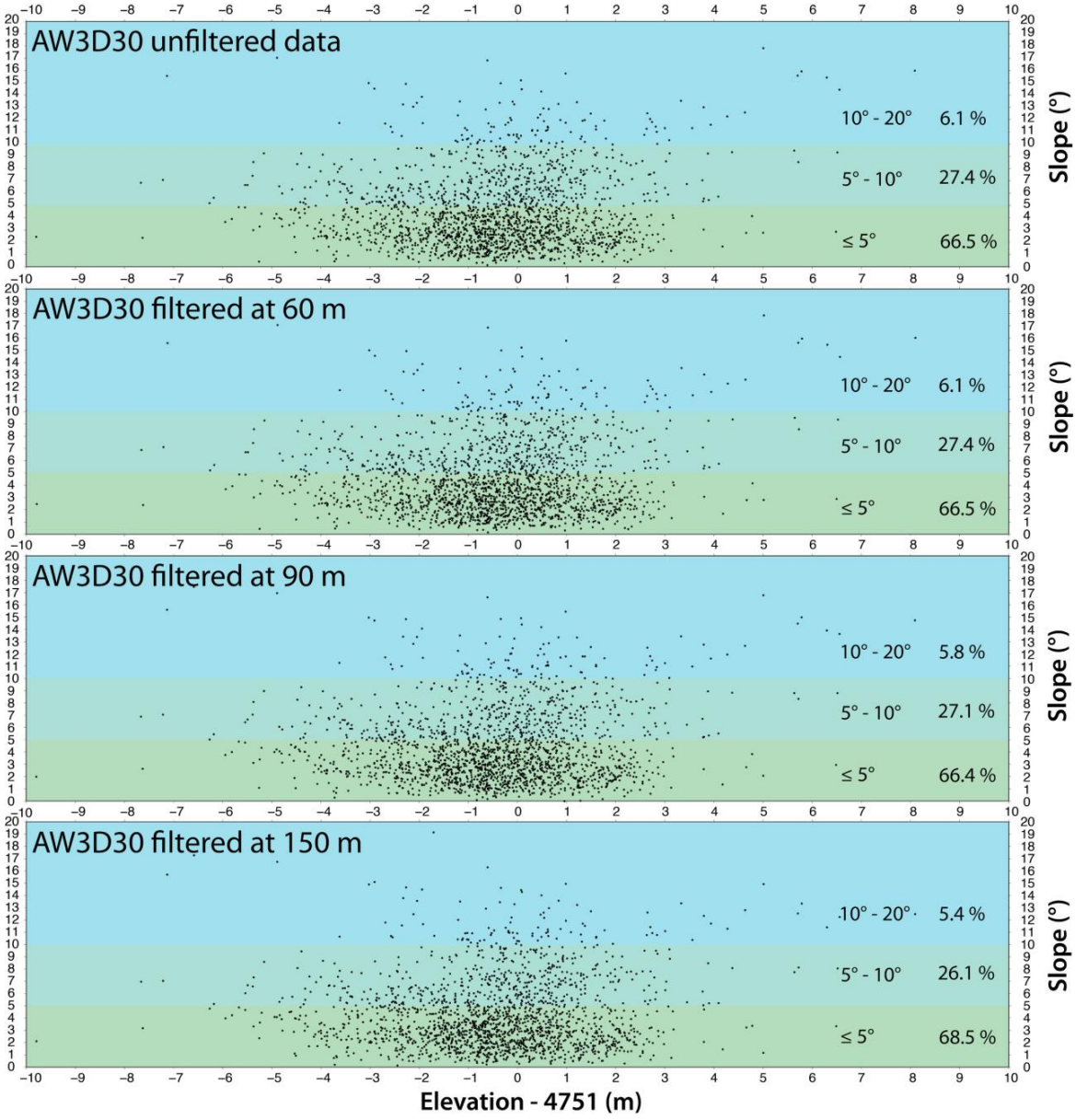
AW3D30 unfiltered data
10° - 20° 6.1 %
5° - 10° 27.4 %
≤ 5° 66.5 %
AW3D30 filtered at 60 m
10° - 20° 6.1 %
5° - 10° 27.4 %
≤ 5° 66.5 %
AW3D30 filtered at 90 m
10° - 20° 5.8 %
5° - 10° 27.1 %
≤ 5° 66.4 %
AW3D30 filtered at 150 m
10° - 20° 5.4 %
5° - 10° 26.1 %
≤ 5° 68.5 %
Slope (°)
Elevation - 4751 (m)

Figure A.2

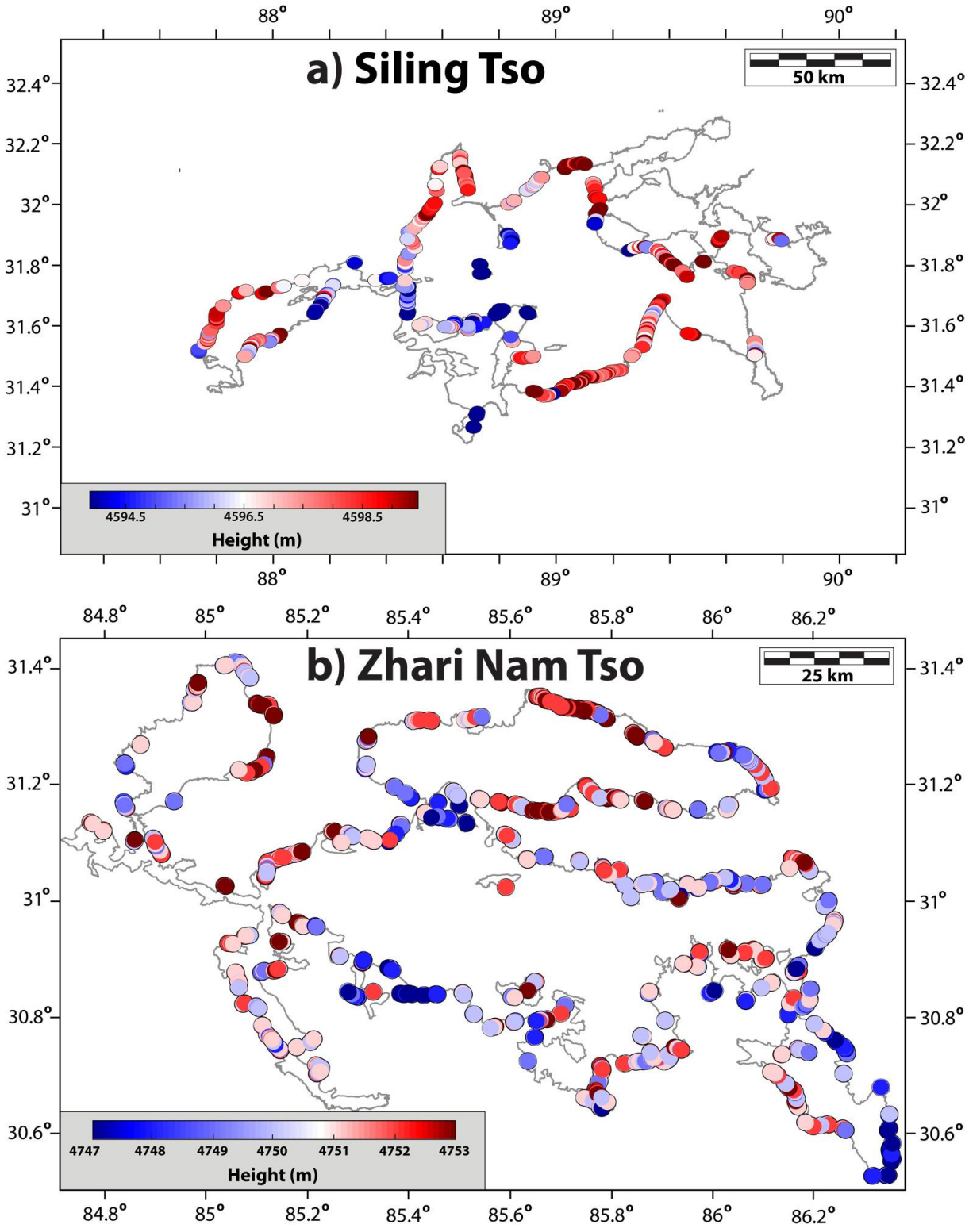
a) Siling Tso
50 km
88°
89°
90°
32.4°
32.2°
32°
31.8°
31.6°
31.4°
31.2°
31°
4594.5
4596.5
4598.5
Height (m)
b) Zhari Nam Tso
25 km
84.8°
85°
85.2°
85.4°
85.6°
85.8°
86°
86.2°
31.4°
31.2°
31°
30.8°
30.6°
4747
4748
4749
4750
4751
4752
4753
Height (m)

Figure A.3

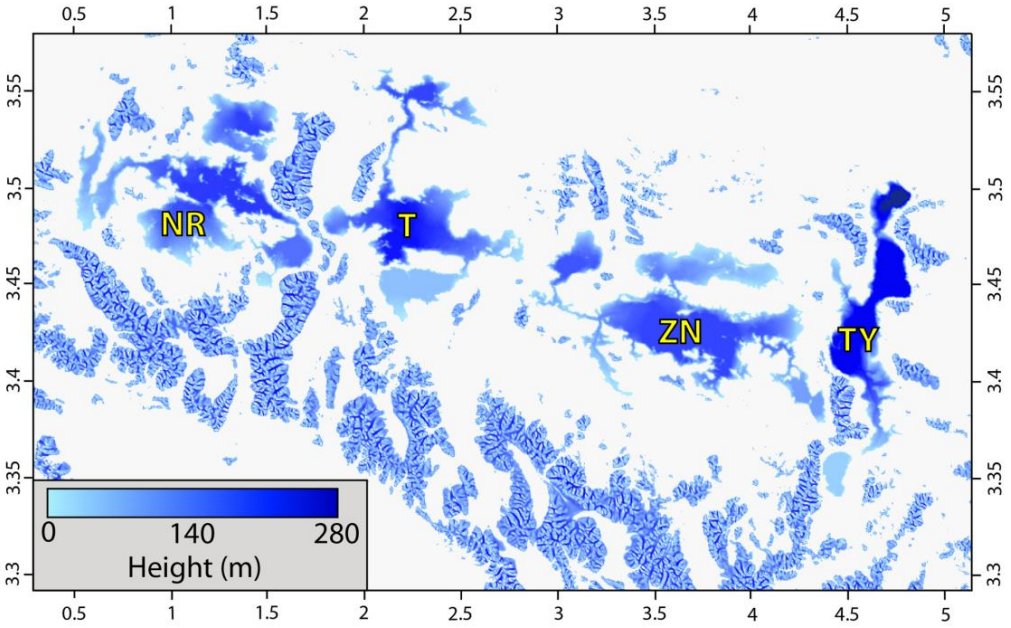

Figure B.1

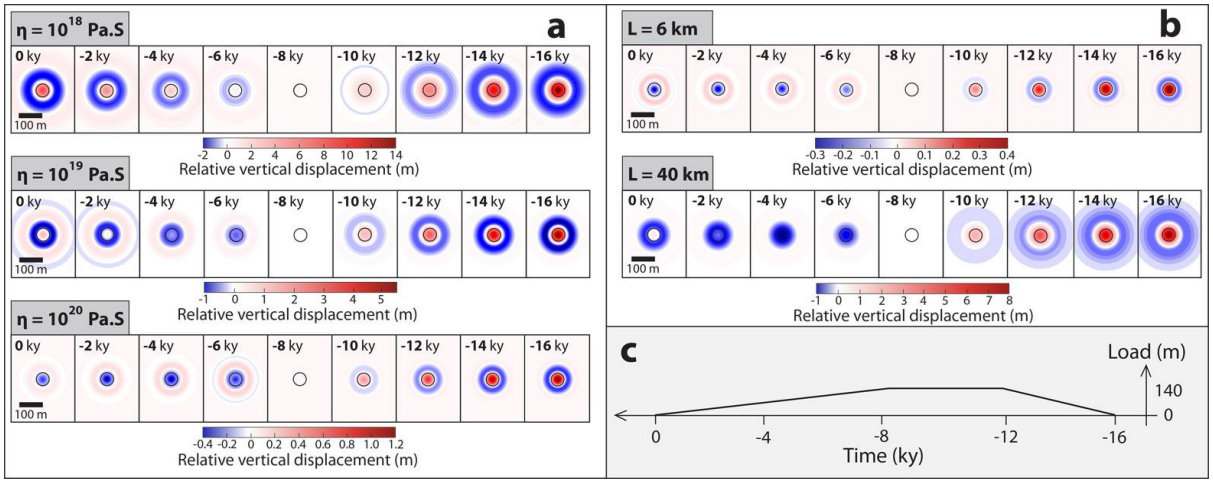

Figure D.1

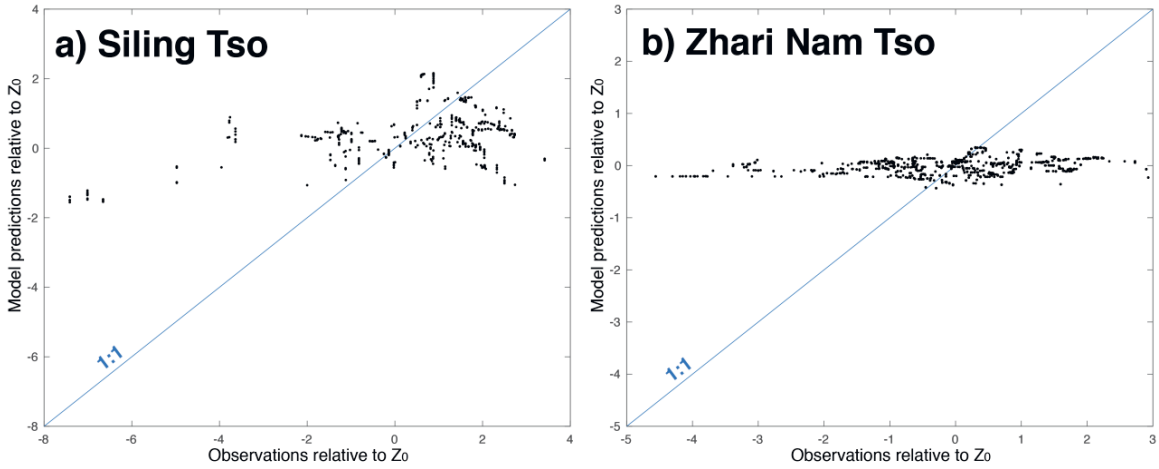
a) Siling Tso
b) Zhari Nam Tso
Model predictions relative to Z0
Observations relative to Z0
1:1

Figure E.1

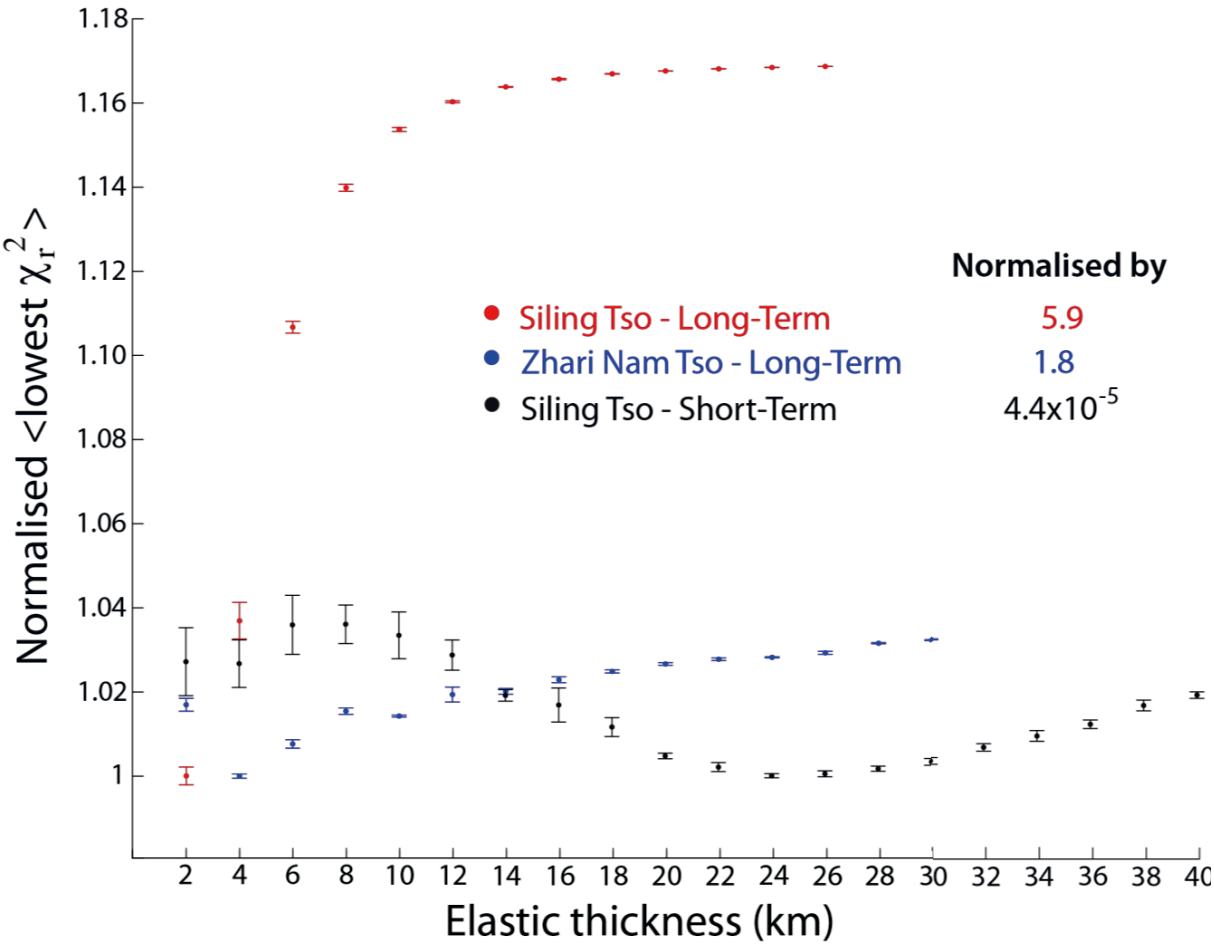
Normalised <lowest χ_r^2>
Elastic thickness (km)
Normalised by
Siling Tso - Long-Term 5.9
Zhari Nam Tso - Long-Term 1.8
Siling Tso - Short-Term 4.4x10-5

Figure E.2

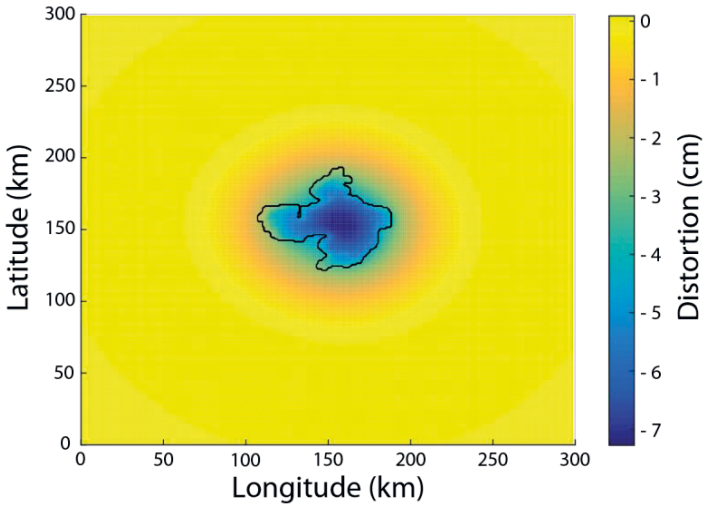

Figure F.1